

Measurement of the top quark mass with the dynamical likelihood method using lepton plus jets events with b -tags in $p\bar{p}$ collisions at $\sqrt{s} = 1.96$ TeV

A. Abulencia,²³ D. Acosta,¹⁷ J. Adelman,¹³ T. Affolder,¹⁰ T. Akimoto,⁵⁴ M. G. Albrow,¹⁶ D. Ambrose,¹⁶ S. Amerio,⁴² D. Amidei,³³ A. Anastassov,⁵¹ K. Anikeev,¹⁶ A. Annovi,⁴⁵ J. Antos,¹ M. Aoki,⁵⁴ G. Apollinari,¹⁶ J.-F. Arguin,³² T. Arisawa,⁵⁶ A. Artikov,¹⁴ W. Ashmanskas,¹⁶ A. Attal,⁸ F. Azfar,⁴¹ P. Azzi-Bacchetta,⁴² P. Azzurri,⁴⁵ N. Bacchetta,⁴² H. Bachacou,²⁸ W. Badgett,¹⁶ A. Barbaro-Galtieri,²⁸ V. E. Barnes,⁴⁷ B. A. Barnett,²⁴ S. Baroiant,⁷ V. Bartsch,³⁰ G. Bauer,³¹ F. Bedeschi,⁴⁵ S. Behari,²⁴ S. Belforte,⁵³ G. Bellettini,⁴⁵ J. Bellinger,⁵⁸ A. Belloni,³¹ E. Ben Haim,⁴³ D. Benjamin,¹⁵ A. Beretvas,¹⁶ J. Beringer,²⁸ T. Berry,²⁹ A. Bhatti,⁴⁹ M. Binkley,¹⁶ D. Bisello,⁴² M. Bishai,¹⁶ R. E. Blair,² C. Blocker,⁶ K. Bloom,³³ B. Blumenfeld,²⁴ A. Bocci,⁴⁹ A. Bodek,⁴⁸ V. Boisvert,⁴⁸ G. Bolla,⁴⁷ A. Bolshov,³¹ D. Bortoletto,⁴⁷ J. Boudreau,⁴⁶ S. Bourov,¹⁶ A. Boveia,¹⁰ B. Brau,¹⁰ C. Bromberg,³⁴ E. Brubaker,¹³ J. Budagov,¹⁴ H. S. Budd,⁴⁸ S. Budd,²³ K. Burkett,¹⁶ G. Busetto,⁴² P. Bussey,²⁰ K. L. Byrum,² S. Cabrera,¹⁵ M. Campanelli,¹⁹ M. Campbell,³³ F. Canelli,⁸ A. Canepa,⁴⁷ D. Carlsmith,⁵⁸ R. Carosi,⁴⁵ S. Carron,¹⁵ M. Casarsa,⁵³ A. Castro,⁵ P. Catastini,⁴⁵ D. Cauz,⁵³ M. Cavalli-Sforza,³ A. Cerri,²⁸ L. Cerrito,⁴¹ S. H. Chang,²⁷ J. Chapman,³³ Y. C. Chen,¹ M. Chertok,⁷ G. Chiarelli,⁴⁵ G. Chlachidze,¹⁴ F. Chlebana,¹⁶ I. Cho,²⁷ K. Cho,²⁷ D. Chokheli,¹⁴ J. P. Chou,²¹ P. H. Chu,²³ S. H. Chuang,⁵⁸ K. Chung,¹² W. H. Chung,⁵⁸ Y. S. Chung,⁴⁸ M. Ciljak,⁴⁵ C. I. Ciobanu,²³ M. A. Ciocci,⁴⁵ A. Clark,¹⁹ D. Clark,⁶ M. Coca,¹⁵ A. Connolly,²⁸ M. E. Convery,⁴⁹ J. Conway,⁷ B. Cooper,³⁰ K. Copic,³³ M. Cordelli,¹⁸ G. Cortiana,⁴² A. Cruz,¹⁷ J. Cuevas,¹¹ R. Culbertson,¹⁶ D. Cyr,⁵⁸ S. DaRonco,⁴² S. D'Auria,²⁰ M. D'onofrio,¹⁹ D. Dagenhart,⁶ P. de Barbaro,⁴⁸ S. De Cecco,⁵⁰ A. Deisher,²⁸ G. De Lentdecker,⁴⁸ M. Dell'Orso,⁴⁵ S. Demers,⁴⁸ L. Demortier,⁴⁹ J. Deng,¹⁵ M. Deninno,⁵ D. De Pedis,⁵⁰ P. F. Derwent,¹⁶ C. Dionisi,⁵⁰ J. R. Dittmann,⁴ P. DiTuro,⁵¹ C. Dörr,²⁵ A. Dominguez,²⁸ S. Donati,⁴⁵ M. Donega,¹⁹ P. Dong,⁸ J. Donini,⁴² T. Dorigo,⁴² S. Dube,⁵¹ K. Ebina,⁵⁶ J. Efron,³⁸ J. Ehlers,¹⁹ R. Erbacher,⁷ D. Errede,²³ S. Errede,²³ R. Eusebi,⁴⁸ H. C. Fang,²⁸ S. Farrington,²⁹ I. Fedorko,⁴⁵ W. T. Fedorko,¹³ R. G. Feild,⁵⁹ M. Feindt,²⁵ J. P. Fernandez,⁴⁷ R. Field,¹⁷ G. Flanagan,³⁴ L. R. Flores-Castillo,⁴⁶ A. Foland,²¹ S. Forrester,⁷ G. W. Foster,¹⁶ M. Franklin,²¹ J. C. Freeman,²⁸ Y. Fujii,²⁶ I. Furic,¹³ A. Gajjar,²⁹ M. Gallinaro,⁴⁹ J. Galyardt,¹² J. E. Garcia,⁴⁵ M. Garcia Sciveres,²⁸ A. F. Garfinkel,⁴⁷ C. Gay,⁵⁹ H. Gerberich,²³ E. Gerchtein,¹² D. Gerdes,³³ S. Giagu,⁵⁰ G. P. di Giovanni,⁴³ P. Giannetti,⁴⁵ A. Gibson,²⁸ K. Gibson,¹² C. Ginsburg,¹⁶ N. Giokaris,¹⁴ K. Giolo,⁴⁷ M. Giordani,⁵³ M. Giunta,⁴⁵ G. Giurgiu,¹² V. Glagolev,¹⁴ D. Glenzinski,¹⁶ M. Gold,³⁶ N. Goldschmidt,³³ J. Goldstein,⁴¹ G. Gomez,¹¹ G. Gomez-Ceballos,¹¹ M. Goncharov,⁵² O. González,⁴⁷ I. Gorelov,³⁶ A. T. Goshaw,¹⁵ Y. Gotra,⁴⁶ K. Goulianos,⁴⁹ A. Gresele,⁴² M. Griffiths,²⁹ S. Grinstein,²¹ C. Grosso-Pilcher,¹³ U. Grundler,²³ J. Guimaraes da Costa,²¹ C. Haber,²⁸ S. R. Hahn,¹⁶ K. Hahn,⁴⁴ E. Halkiadakis,⁴⁸ A. Hamilton,³² B.-Y. Han,⁴⁸ R. Handler,⁵⁸ F. Happacher,¹⁸ K. Hara,⁵⁴ M. Hare,⁵⁵ S. Harper,⁴¹ R. F. Harr,⁵⁷ R. M. Harris,¹⁶ K. Hatakeyama,⁴⁹ J. Hauser,⁸ C. Hays,¹⁵ H. Hayward,²⁹ A. Heijboer,⁴⁴ B. Heinemann,²⁹ J. Heinrich,⁴⁴ M. Henneke,²⁵ M. Herndon,⁵⁸ J. Heuser,²⁵ D. Hidas,¹⁵ C. S. Hill,¹⁰ D. Hirschbuehl,²⁵ A. Hocker,¹⁶ A. Holloway,²¹ S. Hou,¹ M. Houlden,²⁹ S.-C. Hsu,⁹ B. T. Huffman,⁴¹ R. E. Hughes,³⁸ J. Huston,³⁴ K. Ikado,⁵⁶ J. Incandela,¹⁰ G. Introzzi,⁴⁵ M. Iori,⁵⁰ Y. Ishizawa,⁵⁴ A. Ivanov,⁷ B. Iyutin,³¹ E. James,¹⁶ D. Jang,⁵¹ B. Jayatilaka,³³ D. Jeans,⁵⁰ H. Jensen,¹⁶ E. J. Jeon,²⁷ M. Jones,⁴⁷ K. K. Joo,²⁷ S. Y. Jun,¹² T. R. Junk,²³ T. Kamon,⁵² J. Kang,³³ M. Karagöz-Unel,³⁷ P. E. Karchin,⁵⁷ Y. Kato,⁴⁰ Y. Kemp,²⁵ R. Kephart,¹⁶ U. Kerzel,²⁵ V. Khotilovich,⁵² B. Kilminster,³⁸ D. H. Kim,²⁷ H. S. Kim,²⁷ J. E. Kim,²⁷ M. J. Kim,¹² M. S. Kim,²⁷ S. B. Kim,²⁷ S. H. Kim,⁵⁴ Y. K. Kim,¹³ M. Kirby,¹⁵ L. Kirsch,⁶ S. Klimenko,¹⁷ M. Klute,³¹ B. Knuteson,³¹ B. R. Ko,¹⁵ H. Kobayashi,⁵⁴ K. Kondo,⁵⁶ D. J. Kong,²⁷ J. Konigsberg,¹⁷ K. Kordas,¹⁸ A. Korytov,¹⁷ A. V. Kotwal,¹⁵ A. Kovalev,⁴⁴ J. Kraus,²³ I. Kravchenko,³¹ M. Kreps,²⁵ A. Kreymer,¹⁶ J. Kroll,⁴⁴ N. Krumnack,⁴ M. Kruse,¹⁵ V. Krutelyov,⁵² S. E. Kuhlmann,² Y. Kusakabe,⁵⁶ S. Kwang,¹³ A. T. Laasänen,⁴⁷ S. Lai,³² S. Lami,⁴⁵ S. Lammel,¹⁶ M. Lancaster,³⁰ R. L. Lander,⁷ K. Lannon,³⁸ A. Lath,⁵¹ G. Latino,⁴⁵ I. Lazzizzera,⁴² C. Lecci,²⁵ T. LeCompte,² J. Lee,⁴⁸ J. Lee,²⁷ S. W. Lee,⁵² R. Lefèvre,³ N. Leonardo,³¹ S. Leone,⁴⁵ S. Levy,¹³ J. D. Lewis,¹⁶ K. Li,⁵⁹ C. Lin,⁵⁹ C. S. Lin,¹⁶ M. Lindgren,¹⁶ E. Lipeles,⁹ T. M. Liss,²³ A. Lister,¹⁹ D. O. Litvintsev,¹⁶ T. Liu,¹⁶ Y. Liu,¹⁹ N. S. Lockyer,⁴⁴ A. Loginov,³⁵ M. Loretì,⁴² P. Loverre,⁵⁰ R.-S. Lu,¹ D. Lucchesi,⁴² P. Lujan,²⁸ P. Lukens,¹⁶ G. Lungu,¹⁷ L. Lyons,⁴¹ J. Lys,²⁸ R. Lysak,¹ E. Lytken,⁴⁷ P. Mack,²⁵ D. MacQueen,³² R. Madrak,¹⁶ K. Maeshima,¹⁶ P. Maksimovic,²⁴ G. Manca,²⁹ F. Margaroli,⁵ R. Marginean,¹⁶ C. Marino,²³ A. Martin,⁵⁹ M. Martin,²⁴ V. Martin,³⁷ M. Martínez,³ T. Maruyama,⁵⁴ H. Matsunaga,⁵⁴ M. E. Mattson,⁵⁷ R. Mazini,³² P. Mazzanti,⁵ K. S. McFarland,⁴⁸ D. McGivern,³⁰ P. McIntyre,⁵² P. McNamara,⁵¹ R. McNulty,²⁹ A. Mehta,²⁹ S. Menzemer,³¹ A. Menzione,⁴⁵ P. Merkel,⁴⁷ C. Mesropian,⁴⁹ A. Messina,⁵⁰ M. von der Mey,⁸ T. Miao,¹⁶ N. Miladinovic,⁶ J. Miles,³¹ R. Miller,³⁴ J. S. Miller,³³ C. Mills,¹⁰ M. Milnik,²⁵ R. Miquel,²⁸ S. Miscetti,¹⁸ G. Mitselmakher,¹⁷ A. Miyamoto,²⁶ N. Moggi,⁵ B. Mohr,⁸ R. Moore,¹⁶ M. Morello,⁴⁵ P. Movilla Fernandez,²⁸ J. Mülmenstädt,²⁸ A. Mukherjee,¹⁶

M. Mulhearn,³¹ Th. Muller,²⁵ R. Mumford,²⁴ P. Murat,¹⁶ J. Nachtman,¹⁶ S. Nahn,⁵⁹ I. Nakano,³⁹ A. Napier,⁵⁵ D. Naumov,³⁶ V. Neacula,¹⁷ C. Neu,⁴⁴ M. S. Neubauer,⁹ J. Nielsen,²⁸ T. Nigmanov,⁴⁶ L. Nodulman,² O. Norriella,³ T. Ogawa,⁵⁶ S. H. Oh,¹⁵ Y. D. Oh,²⁷ T. Okusawa,⁴⁰ R. Oldeman,²⁹ R. Orava,²² K. Osterberg,²² C. Pagliarone,⁴⁵ E. Palencia,¹¹ R. Paoletti,⁴⁵ V. Papadimitriou,¹⁶ A. Papikononou,²⁵ A. A. Paramonov,¹³ B. Parks,³⁸ S. Pashapour,³² J. Patrick,¹⁶ G. Pauletta,⁵³ M. Paulini,¹² C. Paus,³¹ D. E. Pellett,⁷ A. Penzo,⁵³ T. J. Phillips,¹⁵ G. Piacentino,⁴⁵ J. Piedra,⁴³ K. Pitts,²³ C. Plager,⁸ L. Pondrom,⁵⁸ G. Pope,⁴⁶ X. Portell,³ O. Poukhov,¹⁴ N. Pounder,⁴¹ F. Prakashyn,¹⁴ A. Pronko,¹⁶ J. Proudfoot,² F. Ptohos,¹⁸ G. Punzi,⁴⁵ J. Pursley,²⁴ J. Rademacker,⁴¹ A. Rahaman,⁴⁶ A. Rakitin,³¹ S. Rappoccio,²¹ F. Ratnikov,⁵¹ B. Reiser,¹⁶ V. Rekovic,³⁶ N. van Remortel,²² P. Renton,⁴¹ M. Rescigno,⁵⁰ S. Richter,²⁵ F. Rimondi,⁵ K. Rinnert,²⁵ L. Ristori,⁴⁵ W. J. Robertson,¹⁵ A. Robson,²⁰ T. Rodrigo,¹¹ E. Rogers,²³ S. Rolli,⁵⁵ R. Roser,¹⁶ M. Rossi,⁵³ R. Rossin,¹⁷ C. Rott,⁴⁷ A. Ruiz,¹¹ J. Russ,¹² V. Rusu,¹³ D. Ryan,⁵⁵ H. Saarikko,²² S. Sabik,³² A. Safonov,⁷ W. K. Sakumoto,⁴⁸ G. Salamanna,⁵⁰ O. Salto,³ D. Saltzberg,⁸ C. Sanchez,³ L. Santi,⁵³ S. Sarkar,⁵⁰ K. Sato,⁵⁴ P. Savard,³² A. Savoy-Navarro,⁴³ T. Scheidle,²⁵ P. Schlabach,¹⁶ E. E. Schmidt,¹⁶ M. P. Schmidt,⁵⁹ M. Schmitt,³⁷ T. Schwarz,³³ L. Scodellaro,¹¹ A. L. Scott,¹⁰ A. Scribano,⁴⁵ F. Scuri,⁴⁵ A. Sedov,⁴⁷ S. Seidel,³⁶ Y. Seiya,⁴⁰ A. Semenov,¹⁴ F. Semeria,⁵ L. Sexton-Kennedy,¹⁶ I. Sfiligoi,¹⁸ M. D. Shapiro,²⁸ T. Shears,²⁹ P. F. Shepard,⁴⁶ D. Sherman,²¹ M. Shimojima,⁵⁴ M. Shochet,¹³ Y. Shon,⁵⁸ I. Shreyber,³⁵ A. Sidoti,⁴³ A. Sill,¹⁶ P. Sinervo,³² A. Sisakyan,¹⁴ J. Sjolín,⁴¹ A. Skiba,²⁵ A. J. Slaughter,¹⁶ K. Sliwa,⁵⁵ D. Smirnov,³⁶ J. R. Smith,⁷ F. D. Snider,¹⁶ R. Snihur,³² M. Soderberg,³³ A. Soha,⁷ S. Somalwar,⁵¹ V. Sorin,³⁴ J. Spalding,¹⁶ F. Spinella,⁴⁵ P. Squillacioti,⁴⁵ M. Stanitzki,⁵⁹ A. Staveris-Polykalas,⁴⁵ R. St. Denis,²⁰ B. Stelzer,⁸ O. Stelzer-Chilton,³² D. Stentz,³⁷ J. Strogas,³⁶ D. Stuart,¹⁰ J. S. Suh,²⁷ A. Sukhanov,¹⁷ K. Sumorok,³¹ H. Sun,⁵⁵ T. Suzuki,⁵⁴ A. Taffard,²³ R. Tafirout,³² R. Takashima,³⁹ Y. Takeuchi,⁵⁴ K. Takikawa,⁵⁴ M. Tanaka,² R. Tanaka,³⁹ M. Tecchio,³³ P. K. Teng,¹ K. Terashi,⁴⁹ S. Tether,³¹ J. Thom,¹⁶ A. S. Thompson,²⁰ E. Thomson,⁴⁴ P. Tipton,⁴⁸ V. Tiwari,¹² S. Tkaczyk,¹⁶ D. Toback,⁵² S. Tokar,¹⁴ K. Tollefson,³⁴ T. Tomura,⁵⁴ D. Tonelli,⁴⁵ M. Tönnemann,³⁴ S. Torre,⁴⁵ D. Torretta,¹⁶ S. Tourneur,⁴³ W. Trischuk,³² R. Tsuchiya,⁵⁶ S. Tsuno,³⁹ N. Turini,⁴⁵ F. Ukegawa,⁵⁴ T. Unverhau,²⁰ S. Uozumi,⁵⁴ D. Usynin,⁴⁴ L. Vacavant,²⁸ A. Vaiciulis,⁴⁸ S. Vallecorsa,¹⁹ A. Varganov,³³ E. Vataga,³⁶ G. Velev,¹⁶ G. Veramendi,²³ V. Veszpremi,⁴⁷ T. Vickey,²³ R. Vidal,¹⁶ I. Vila,¹¹ R. Vilar,¹¹ I. Vollrath,³² I. Volobouev,²⁸ F. Würthwein,⁹ P. Wagner,⁵² R. G. Wagner,² R. L. Wagner,¹⁶ W. Wagner,²⁵ R. Wallny,⁸ T. Walter,²⁵ Z. Wan,⁵¹ M. J. Wang,¹ S. M. Wang,¹⁷ A. Warburton,³² B. Ward,²⁰ S. Waschke,²⁰ D. Waters,³⁰ T. Watts,⁵¹ M. Weber,²⁸ W. C. Wester III,¹⁶ B. Whitehouse,⁵⁵ D. Whiteson,⁴⁴ A. B. Wicklund,² E. Wicklund,¹⁶ H. H. Williams,⁴⁴ P. Wilson,¹⁶ B. L. Winer,³⁸ P. Wittich,⁴⁴ S. Wolbers,¹⁶ C. Wolfe,¹³ S. Worm,⁵¹ T. Wright,³³ X. Wu,¹⁹ S. M. Wynne,²⁹ A. Yagil,¹⁶ K. Yamamoto,⁴⁰ J. Yamaoka,⁵¹ Y. Yamashita,³⁹ C. Yang,⁵⁹ U. K. Yang,¹³ W. M. Yao,²⁸ G. P. Yeh,¹⁶ J. Yoh,¹⁶ K. Yorita,¹³ T. Yoshida,⁴⁰ I. Yu,²⁷ S. S. Yu,⁴⁴ J. C. Yun,¹⁶ L. Zanello,⁵⁰ A. Zanetti,⁵³ I. Zaw,²¹ F. Zetti,⁴⁵ X. Zhang,²³ J. Zhou,⁵¹ and S. Zucchelli⁵

(CDF Collaboration)

¹*Institute of Physics, Academia Sinica, Taipei, Taiwan 11529, Republic of China*²*Argonne National Laboratory, Argonne, Illinois 60439, USA*³*Institut de Física d'Altes Energies, Universitat Autònoma de Barcelona, E-08193, Bellaterra (Barcelona), Spain*⁴*Baylor University, Waco, Texas 76798, USA*⁵*Istituto Nazionale di Fisica Nucleare, University of Bologna, I-40127 Bologna, Italy*⁶*Brandeis University, Waltham, Massachusetts 02254, USA*⁷*University of California, Davis, Davis, California 95616, USA*⁸*University of California, Los Angeles, Los Angeles, California 90024, USA*⁹*University of California, San Diego, La Jolla, California 92093, USA*¹⁰*University of California, Santa Barbara, Santa Barbara, California 93106, USA*¹¹*Instituto de Física de Cantabria, CSIC-University of Cantabria, 39005 Santander, Spain*¹²*Carnegie Mellon University, Pittsburgh, Pennsylvania 15213, USA*¹³*Enrico Fermi Institute, University of Chicago, Chicago, Illinois 60637, USA*¹⁴*Joint Institute for Nuclear Research, RU-141980 Dubna, Russia*¹⁵*Duke University, Durham, North Carolina 27708, USA*¹⁶*Fermi National Accelerator Laboratory, Batavia, Illinois 60510, USA*¹⁷*University of Florida, Gainesville, Florida 32611, USA*¹⁸*Laboratori Nazionali di Frascati, Istituto Nazionale di Fisica Nucleare, I-00044 Frascati, Italy*

- ¹⁹University of Geneva, CH-1211 Geneva 4, Switzerland
²⁰Glasgow University, Glasgow G12 8QQ, United Kingdom
²¹Harvard University, Cambridge, Massachusetts 02138, USA
²²Division of High Energy Physics, Department of Physics, University of Helsinki and Helsinki Institute of Physics, FIN-00014, Helsinki, Finland
²³University of Illinois, Urbana, Illinois 61801, USA
²⁴The Johns Hopkins University, Baltimore, Maryland 21218, USA
²⁵Institut für Experimentelle Kernphysik, Universität Karlsruhe, 76128 Karlsruhe, Germany
²⁶High Energy Accelerator Research Organization (KEK), Tsukuba, Ibaraki 305, Japan
²⁷Center for High Energy Physics: Kyungpook National University, Taegu 702-701; Seoul National University, Seoul 151-742; and SungKyunKwan University, Suwon 440-746, Korea
²⁸Ernest Orlando Lawrence Berkeley National Laboratory, Berkeley, California 94720, USA
²⁹University of Liverpool, Liverpool L69 7ZE, United Kingdom
³⁰University College London, London WC1E 6BT, United Kingdom
³¹Massachusetts Institute of Technology, Cambridge, Massachusetts 02139, USA
³²Institute of Particle Physics: McGill University, Montréal, Canada H3A 2T8; and University of Toronto, Toronto, Canada M5S 1A7
³³University of Michigan, Ann Arbor, Michigan 48109, USA
³⁴Michigan State University, East Lansing, Michigan 48824, USA
³⁵Institution for Theoretical and Experimental Physics, ITEP, Moscow 117259, Russia
³⁶University of New Mexico, Albuquerque, New Mexico 87131, USA
³⁷Northwestern University, Evanston, Illinois 60208, USA
³⁸The Ohio State University, Columbus, Ohio 43210, USA
³⁹Okayama University, Okayama 700-8530, Japan
⁴⁰Osaka City University, Osaka 588, Japan
⁴¹University of Oxford, Oxford OX1 3RH, United Kingdom
⁴²University of Padova, Istituto Nazionale di Fisica Nucleare, Sezione di Padova-Trento, I-35131 Padova, Italy
⁴³LPNHE-Universite de Paris 6/IN2P3-CNRS
⁴⁴University of Pennsylvania, Philadelphia, Pennsylvania 19104, USA
⁴⁵Istituto Nazionale di Fisica Nucleare Pisa, Universities of Pisa, Siena and Scuola Normale Superiore, I-56127 Pisa, Italy
⁴⁶University of Pittsburgh, Pittsburgh, Pennsylvania 15260, USA
⁴⁷Purdue University, West Lafayette, Indiana 47907, USA
⁴⁸University of Rochester, Rochester, New York 14627, USA
⁴⁹The Rockefeller University, New York, New York 10021, USA
⁵⁰Istituto Nazionale di Fisica Nucleare, Sezione di Roma 1, University of Rome “La Sapienza,” I-00185 Roma, Italy
⁵¹Rutgers University, Piscataway, New Jersey 08855, USA
⁵²Texas A&M University, College Station, Texas 77843, USA
⁵³Istituto Nazionale di Fisica Nucleare, University of Trieste/ Udine, Italy
⁵⁴University of Tsukuba, Tsukuba, Ibaraki 305, Japan
⁵⁵Tufts University, Medford, Massachusetts 02155, USA
⁵⁶Waseda University, Tokyo 169, Japan
⁵⁷Wayne State University, Detroit, Michigan 48201, USA
⁵⁸University of Wisconsin, Madison, Wisconsin 53706, USA
⁵⁹Yale University, New Haven, Connecticut 06520, USA

(Received 6 December 2005; published 10 May 2006)

This paper describes a measurement of the top quark mass, M_{top} , with the dynamical likelihood method (DLM) using the CDF II detector at the Fermilab Tevatron. The Tevatron produces top/antitop ($t\bar{t}$) pairs in $p\bar{p}$ collisions at a center-of-mass energy of 1.96 TeV. The data sample used in this analysis was accumulated from March 2002 through August 2004, which corresponds to an integrated luminosity of 318 pb^{-1} . We use the $t\bar{t}$ candidates in the “lepton + jets” decay channel, requiring at least one jet identified as a b quark by finding a displaced secondary vertex. The DLM defines a likelihood for each event based on the differential cross section as a function of M_{top} per unit phase space volume of the final partons, multiplied by the transfer functions from jet to parton energies. The method takes into account all possible jet combinations in an event, and the likelihood is multiplied event by event to derive the top quark mass by the maximum likelihood method. Using 63 $t\bar{t}$ candidates observed in the data, with 9.2 events expected from background, we measure the top quark mass to be $173.2^{+2.6}_{-2.4}(\text{stat.}) \pm 3.2(\text{sys.}) \text{ GeV}/c^2$, or $173.2^{+4.1}_{-4.0} \text{ GeV}/c^2$.

I. INTRODUCTION

The top quark mass is an important quantity in particle physics. Its precise value not only serves for setting basic parameters in calculations of electroweak processes, but also provides a constraint on the mass of the Higgs boson. Therefore it is desirable to have a measurement with a precision comparable to that of other relevant electroweak parameters, typically of the order of 0.1%–1%, the latter corresponding to about 2 GeV/ c^2 in M_{top} . Based on Run I Tevatron data at a center-of-mass energy of 1.8 TeV (1992–1996), the CDF and D0 collaborations published several direct experimental measurements of M_{top} with all decay topologies arising from $t\bar{t}$ production: the dilepton channel [1,2], the lepton + jets channel [3,4], and the all-jets channel [5,6]. Including a recent reanalysis of D0 Run I data [7], the Run I world average top quark mass is 178.0 ± 4.3 GeV/ c^2 [8]. A global standard model fit using this updated value gives the most likely value of the Higgs boson mass of 129^{+74}_{-49} GeV/ c^2 , and the 95% C.L. upper limit of 285 GeV/ c^2 [9].

In this paper we present a measurement of the top quark mass in $p\bar{p}$ collisions at $\sqrt{s} = 1.96$ TeV at the Fermilab Tevatron. The data were obtained with the upgraded collider detector at Fermilab (CDF II) operated during Run II. The integrated luminosity of the data sample, collected from March 2002 through August 2004, is 318 pb $^{-1}$. This is the total data set for which all detectors including the silicon tracker were operating. The method employed is the dynamical likelihood method (DLM) [10–13], which uses the differential cross section for the $t\bar{t}$ process as a function of M_{top} in the likelihood definition. The permutations in assigning jets to the primary quarks from the t and \bar{t} decays and the quadratic ambiguity in the z component of the neutrino momentum are incorporated in the likelihood for an event, and the likelihood is multiplied event by event to extract M_{top} by the maximum likelihood method. Similar but not identical techniques were introduced and employed during Run I [7,14,15]. Using Run II data, CDF recently produced the best single top quark mass measurement using the template method with *in situ* jet energy calibration [16]. That analysis and this one are summarized together in [17].

In this method, we assume that the standard model (SM) accurately describes $t\bar{t}$ production and decay. This assumption is justified for two reasons: (1) Since the discovery of the top quark was established in Run I [18], its properties have been investigated using both Run I and Run II data, but no significant discrepancies between experimental data and the SM have been found [19–21]. (2) The SM neither predicts the top quark mass directly, nor explains why it is approximately 40 times more massive than the b quark, the isodoublet partner of the top quark. Therefore it is reasonable to use the SM in the likelihood definition (through the differential cross section) for the mass measurement.

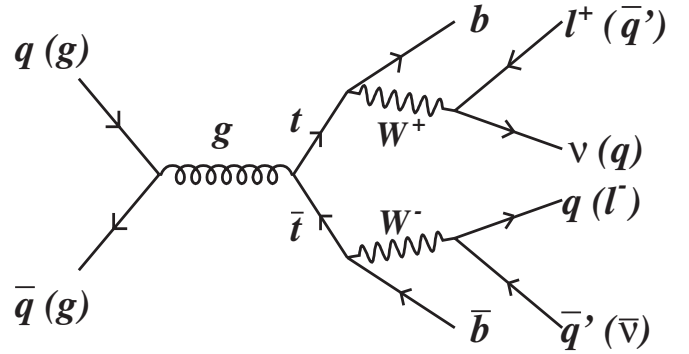


FIG. 1. Tree-level Feynman diagram of standard model $t\bar{t}$ production and decay in the lepton + jets mode.

According to the SM, the top quark decays approximately 100% of the time into a W boson and a b quark. The W then decays to a quark-antiquark or lepton-neutrino pair. The measurement presented here uses events with $t\bar{t}$ decaying in the “lepton + jets” channel, $t\bar{t} \rightarrow W^+ W^- b\bar{b} \rightarrow l\nu q\bar{q}' b\bar{b}$, as shown in Fig. 1, which provided the most accurate mass measurement in Run I because of higher statistics than the dilepton channel and lower background than the all-jets channel. This channel is characterized by a single high p_T lepton (electron or muon) and missing transverse energy from a $W \rightarrow l\nu$ decay, plus four jets, two from the hadronically decaying W boson and two b quarks from the top decays. The b quarks may be identified (“ b -tagged”) by reconstructing secondary vertices from the decay of B hadrons with the silicon vertex detector (SECVTX tagging), as described in Sec. IV C.

This paper is organized as follows. In Sec. II, we present a brief description of the most important detector subsystems to this analysis. Section III describes the data samples that are used in the top quark mass measurement. Section IV presents particle identification and event selection. The background estimates are described in Sec. V. After a brief overview of the DLM procedure in Sec. VI, the definition of the dynamical likelihood function and the reconstruction procedure are discussed in Sec. VII. The transfer functions between jet and parton kinematics, which play a key role in the method, are presented in Sec. VIII. Section IX describes top quark mass determination studies using Monte Carlo (MC) for both the $t\bar{t}$ signal and background events. The effect of background on the likelihood distribution is also investigated. Section X presents the final top quark mass result after correcting for the mass-pulling effect of the background. Section XI discusses further checks on this analysis. The systematic uncertainties are presented in Sec. XII. Conclusions are summarized in Sec. XIII.

II. THE CDF DETECTOR OVERVIEW

The CDF II detector, a general purpose detector with azimuthal and forward-backward symmetry, is composed

of independent subsystems designed for distinct tasks relating to the study of $p\bar{p}$ interactions.

The CDF coordinate system consists of the z axis along the proton beam direction, the azimuthal angle ϕ defined in the plane transverse to the z axis, and the polar angle θ from the proton direction [usually expressed as the pseudorapidity $\eta = -\ln(\tan(\theta/2))$]. The x and y axes point outward and upward from the Tevatron ring, respectively. Transverse energy (E_T) and momentum (p_T) are defined in this plane, perpendicular to the z axis.

The three most relevant subsystems to $t\bar{t} \rightarrow$ lepton + jets event detection are the tracking chambers, the calorimeters, and the muon chambers. These subsystems are briefly described below. A complete description of the CDF II detector can be found elsewhere [22].

The tracking system consists of a large open-cell drift chamber and silicon microstrip detectors. These lie inside a superconducting solenoid of length 5 m and diameter 3.2 m, which produces a 1.4 T magnetic field aligned coaxially with the beam pipe, and are used for measuring charged particle momenta. The outermost system, the central outer tracker (COT) is a 3.1 m long open-cell drift chamber which provides 96 position measurements in the radial region between 0.43 and 1.32 m [23] and in the pseudorapidity region $|\eta| \leq 1.0$. Sense wires are arranged in 8 alternating axial and $\pm 2^\circ$ stereo superlayers with 12 wires each. The position resolution of a single drift time measurement is approximately $140 \mu\text{m}$. Between the interaction region and the COT, there are three separate silicon detectors. In combination, silicon detectors provide high resolution position measurements for charged particles out to $|\eta| = 2.0$. The innermost device, layer 00 [24], is a single-sided layer of silicon microstrip detectors mounted directly on the beam pipe at a radius of 1.6 cm that provides an axial measurement as close to the collision point as possible. Between the COT and layer 00, a five-layer double-sided silicon detector (SVXII) covers the radial region between 2.4 and 10.7 cm [25]. Three separate SVX barrel modules are located along the beam line, covering a length of 96 cm. Three of the five layers combine an r - ϕ measurement on one side and a 90° stereo measurement on the other, and the remaining two layers combine r - ϕ with small-angle stereo at $\pm 1.2^\circ$. The typical hit resolution is $11 \mu\text{m}$. Three additional layers of double-sided silicon strips, the intermediate silicon layers (ISL), are located at larger radii, between 19 and 30 cm, and provide good linking between tracks in the COT and SVXII [26].

Outside of the tracking systems and the solenoid, segmented electromagnetic (EM) and hadronic (Had) sampling calorimeters are used to reconstruct electromagnetic showers and jets in the pseudorapidity interval $|\eta| < 3.6$ [27–29]. The calorimeters are segmented into projective towers of size 7.5° – 15° in ϕ and 0.1 in η . At the front of each tower, a lead-scintillator sampling electromagnetic

calorimeter, 18 radiation lengths deep, records the energy of electromagnetic showers. In the central region ($|\eta| < 1.0$), a layer of multiwire proportional chambers (CES) measures the transverse shower profile at a depth of the maximum shower development. Behind the electromagnetic calorimeter is the hadronic calorimeter with roughly 5 absorption lengths of alternating layers of steel and scintillator.

High p_T muons used in this analysis are detected in three separate subdetectors. Two separated drift chambers cover the region $|\eta| \leq 0.6$: Directly outside of the hadron calorimeter, four-layer stacks of planar drift chambers (CMU) detect muons with $p_T > 1.4 \text{ GeV}/c$ which penetrate the five absorption lengths of the calorimeter [30]. Behind another 60 cm of steel, an additional four layers (CMP) detect muons with $p_T > 2.0 \text{ GeV}/c$ [31]. An additional system with 4 drift chamber layers and scintillation counters occupies the region $0.6 \leq |\eta| \leq 1.0$ (CMX), completing the muon coverage over the full fiducial region of COT tracking, $|\eta| \leq 1.0$.

III. DATA SAMPLES

A. Luminosity and triggers

The results reported here are based on the data recorded during the period March 2002–August 2004, when the average instantaneous Tevatron luminosity was approximately $4 \times 10^{31} \text{ cm}^{-2} \text{ s}^{-1}$, and the highest was about $10 \times 10^{31} \text{ cm}^{-2} \text{ s}^{-1}$. The recorded integrated luminosity for this period is $318 \pm 19 \text{ pb}^{-1}$ for electron and CMU/CMP muon analysis, and $305 \pm 18 \text{ pb}^{-1}$ for CMX muon analysis.

CDF employs a three-level trigger system. We describe only the triggers important for this analysis, which select events containing a high-momentum electron or muon. For electron candidates, the first level (L1) trigger requires a track with $p_T \geq 8 \text{ GeV}/c$ matched to an EM calorimeter cell with $E_T \geq 8 \text{ GeV}$, and a ratio of hadronic to electromagnetic energy ($E_{\text{Had}}/E_{\text{EM}}$) less than 0.125. Calorimeter clustering is done in the second level (L2) trigger, which requires a track with $p_T \geq 8 \text{ GeV}/c$ matched to an EM cluster with $E_T \geq 16 \text{ GeV}$. At the third level (L3), a reconstructed electron with $E_T > 18 \text{ GeV}$ is required. For muon candidates, a track with $p_T \geq 8 \text{ GeV}/c$ matched to muon stubs in the muon chambers (CMU, CMP, or CMX) is required for L1 and L2; the L3 trigger requires a $p_T \geq 18 \text{ GeV}/c$ track.

B. Monte Carlo programs

The generation of $t\bar{t}$ events relies mainly on the HERWIG V6.505 [32] and PYTHIA V6.216 [33] Monte Carlo programs, which employ leading-order QCD matrix elements for the hard process, followed by parton showering to simulate gluon radiation and fragmentation. The CTEQ5L [34] parton distribution functions are used. For heavy flavor jets, the

decay algorithm QQ V9.1 [35] is used to provide proper modeling of bottom and charm hadron decays. The ALPGEN V1.3 program [36], which generates high multiplicity parton final states using exact leading-order matrix elements, is used in the study of backgrounds. The parton level events are then passed to HERWIG and QQ for additional QCD radiation, fragmentation, and B hadron decay.

The CDF II detector simulation [37] reproduces the response of the detector to particles produced in $p\bar{p}$ collisions. Tracking of particles through matter is performed with GEANT3 [38]. Charge deposition in the silicon detectors is calculated using a parametric model tuned to the existing data. The drift model for the COT uses the GARFIELD package [23], with the default parameters tuned to match COT data. The calorimeter simulation uses the GFLASH [39] parametrization package interfaced with GEANT3. The GFLASH parameters are tuned to test-beam data for electrons and pions, and are checked by comparing the calorimeter energy of isolated tracks in $p\bar{p}$ collision data to their momenta as measured in the COT.

IV. PARTICLE IDENTIFICATION AND EVENT SELECTION

A. Lepton identification

The identification of charged leptons produced by W decay provides the initial selection of the $t\bar{t} \rightarrow$ lepton + jets sample. After passing the trigger requirements, electron candidates are identified by requiring the electrons to be in the central pseudorapidity region of the detector ($|\eta| \leq 1$) and to have an EM cluster with $E_T \geq 20$ GeV and a track with $p_T \geq 10$ GeV/ c . Several variables are used to discriminate against charged hadrons and photon conversions. We require that the extrapolated track match the shower location as measured in the CES, that the ratio of hadronic to electromagnetic energy in the calorimeter cluster, $E_{\text{Had}}/E_{\text{EM}}$, be less than $0.055 + 0.00045 \times E_{\text{EM}}$, and that the ratio of cluster energy to track momentum, E/p , be less than 2.0 (unless $p_T > 50$ GeV/ c , in which case this cut is not applied). The isolation variable, defined as the ratio of the additional energy deposited in a cone of radius $\Delta R \equiv \sqrt{\Delta\eta^2 + \Delta\phi^2} = 0.4$ around the electron cluster to the electron energy, is required to be less than 0.1. Conversion electrons are removed by rejecting events that have a pair of opposite electric charge tracks (one of them the electron) in which the distance $\Delta(xy)$ between the tracks in the r - ϕ plane (at the conversion point) is less than 0.2 cm, and the difference between the polar angle cotangent of the two tracks, $|\Delta \cot\theta|$, is less than 0.04. Fiducial cuts on the electromagnetic shower position in the CES ensure that the shower is located in a well-understood region of the calorimeter. For isolated high-momentum electrons from W decay, the tracking efficiency is measured to be $99.93^{+0.07}_{-0.35}$ % [40]. The transverse energy can

be measured from the electromagnetic cluster with a precision $\sigma/E_T = 13.5\%/\sqrt{E_T(\text{GeV})} \oplus 2\%$ [27].

Muon candidates are identified by extrapolating COT tracks to the muon detectors. Two types of high- p_T muon samples are used in this analysis. CMUP muons ($|\eta| \leq 0.6$) have a COT track linked to track segments in both CMU and CMP. A CMX muon ($0.6 \leq |\eta| \leq 1.0$) has a COT track linked to a track segment in the CMX. For both CMUP and CMX muons, we require that the COT track has $p_T \geq 20$ GeV/ c , and that the energy in the calorimeter tower containing the muon is consistent with the deposit expected from a minimum ionizing particle. The latter rejects secondary particles in calorimeter hadron showers that produce tracks in the muon chambers. An isolation variable is defined as the ratio of the total energy deposited in a cone of radius $\Delta R = 0.4$ around the muon track candidate (excluding the towers the muon passed through) to the track momentum, and is required to be less than 0.1. Backgrounds from cosmic rays are removed by requiring that the distance d of closest approach of the reconstructed track to the beam line be less than 0.2 cm. For high-momentum COT tracks, the resolution at the origin is $\delta z \approx 0.5$ cm along the beam line and $\delta d \approx 350 \mu\text{m}$ ($\approx 40 \mu\text{m}$ with SVXII) for the impact parameter in the transverse plane. Additionally, the distance between the extrapolated track and the track segment in the muon chamber is required to be less than 3, 5, and 6 cm for CMU, CMP, and CMX, respectively. COT tracks are required to have at least 3 axial and 2 stereo layers with at least 5 hits each for both electron and muon candidates. From the COT, the transverse momentum resolution for high-momentum particles is found to be $\delta p_T/p_T \approx 0.15\% \times p_T$ (GeV/ c).

B. Jet corrections and systematics

Jet reconstruction in this paper employs a cone cluster algorithm with cone radius $\Delta R \equiv \sqrt{\Delta\eta^2 + \Delta\phi^2} = 0.4$ [41]. We measure the transverse energy $E_T = E \sin\theta$, where θ is the polar angle of the centroid of the cluster's towers, calculated using the measured z position of the event vertex. The total energy E is the sum of the energy deposited in calorimeter towers within the cone. Jets are identified as isolated clusters that contain significant hadronic energy. Jet measurements make the largest contribution to the resolution of the top quark mass reconstruction due to their relatively poor energy resolution, approximately $(0.1 \times E_T + 1.0)$ GeV [42]. Additionally, the uncertainty arising from the jet energy scale is the dominant source of systematic uncertainty for the top quark mass. In contrast, we assume the angles of the quarks are well measured from the jet angles. They are therefore directly used in the mass reconstruction without correction. We briefly describe the jet energy corrections and their systematic uncertainties in this section. More details on the CDF jet energy response are available elsewhere [43].

1. Jet corrections

To be used for top quark mass reconstruction, measured jet energies are first corrected with a set of “flavor-independent” or “generic” corrections, so called because they are extracted mainly from dijet and minimum bias samples. These corrections are made in several steps. A first correction scales the forward calorimeters to the central calorimeter ($0.2 < |\eta| < 0.6$) scale for data and Monte Carlo separately. A dijet balancing procedure is used based on the equality of the transverse energies of the two jets in a $2 \rightarrow 2$ process. The correction is obtained as a function of η and the transverse momentum, p_T , of the jet. The relative correction ranges from about -10% to $+15\%$. The corrections are tested by comparing E_T balance in $\gamma + \text{jet}$ events in data and Monte Carlo simulations. As shown in Fig. 2, after corrections the response of the calorimeter is almost flat with respect to η for both data and Monte Carlo simulations. A second correction is for multiple $p\bar{p}$ interactions due to high-luminosity operation of the Tevatron. The energy from additional $p\bar{p}$ interactions during the same accelerator bunch crossing can fall inside a jet cluster, increasing the energy of the measured jet. The correction associated with this effect is derived from minimum bias data and is parametrized as a function of the number of identified interaction vertices in the event. This effect is corrected on average and is very small (less than 1%). A third correction is called the absolute energy correction. This correction is applied to account for calorimeter nonlinearity and is based on the response of the calorimeter to individual hadrons as measured by E/p of single tracks in the data. After this, the jet energy corresponds to the energy of the incident hadrons on the jet cone. The absolute correction varies between $+10\%$ and $+40\%$, depending on the jet p_T as shown in Fig. 3. The

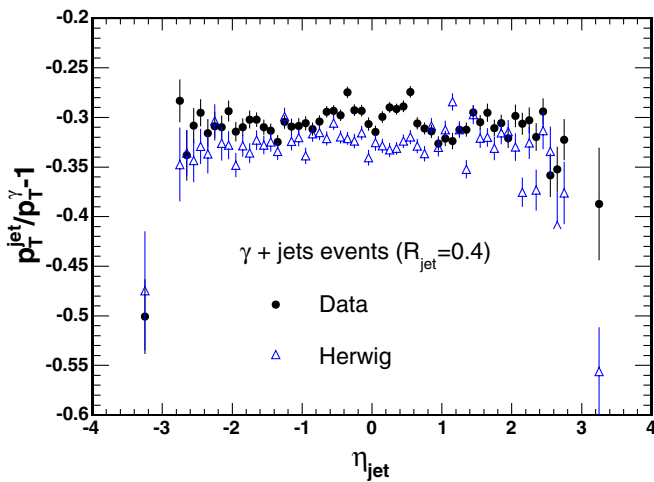


FIG. 2 (color online). p_T balance, $p_T^{\text{jet}, \gamma} / p_T^\gamma - 1$, in γ -jet events as a function of jet η after relative corrections are applied. Circles are data and HERWIG Monte Carlo simulation is plotted as triangles.

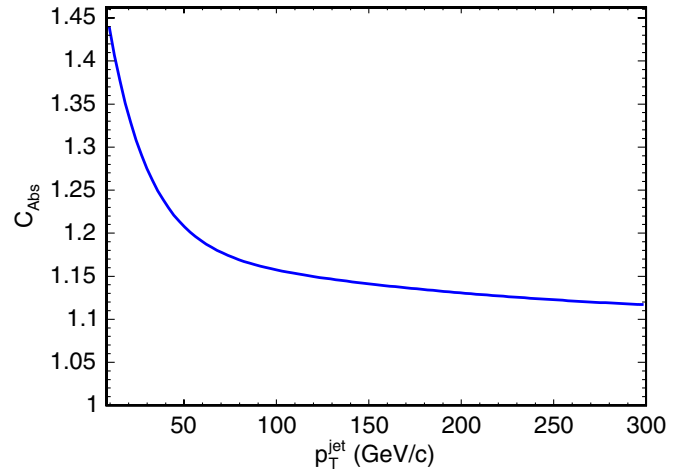


FIG. 3 (color online). The size of the absolute (hadron level) correction, C_{Abs} , as a function of p_T of the jet for cone size 0.4.

accuracy of this correction depends on the Monte Carlo correctly modeling jet fragmentation into hadrons, for example, the charged to neutral particle ratio, and the particle multiplicity and p_T spectrum. This has been checked by comparing the jet charged particle multiplicity distributions in data and Monte Carlo.

After these generic jet energy corrections, we use the transfer functions described in Sec. VIII to account for the fraction of the quark energy deposited outside the jet cone as well as differences between light quark jets from W boson decay and the b jets coming directly from the top quark decay. Since the transfer functions are evaluated as a function of E_T , the resulting top quark mass is insensitive to the difference in the E_T distributions of the dijet and top quark events.

2. Systematics uncertainty on the jet energy scale

The systematic uncertainty on the jet energy scale comes from a number of sources. The uncertainty in the calorimeter response relative to the central calorimeter (relative response) is determined by varying the dijet event selection criteria and the fitting procedure. This uncertainty is typically between 0.5% and 1.0% for most jets used in the top quark mass analysis. A second systematic uncertainty comes from the hadron jet modeling used in the absolute energy scale correction. The main sources here are uncertainties in the calorimeter response to single hadrons (E/p) and jet fragmentation (charged to neutral particle ratio). Smaller contributions come from the Monte Carlo modeling of the calorimeter response close to tower boundaries in azimuth, and from the stability of the calorimeter calibration with time. In total, this uncertainty ranges from 1.5% to 3.0%, depending on jet p_T .

A third systematic uncertainty arises from modeling the energy that is deposited outside the jet cone (out-of-cone correction). This uncertainty, which ranges from 2% to 6% depending on jet p_T , is determined from the difference

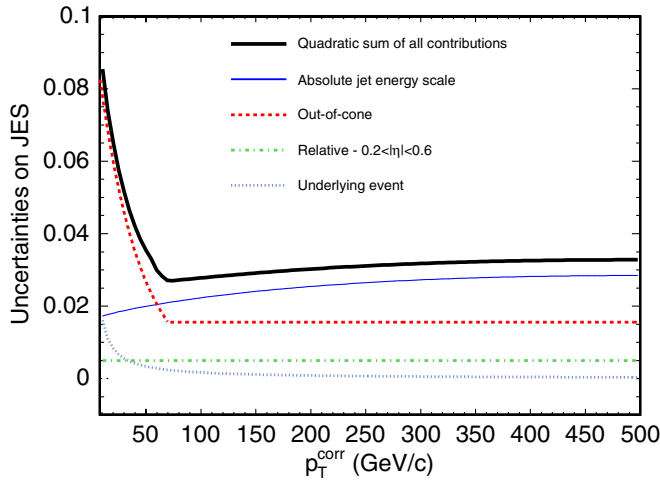


FIG. 4 (color online). The systematic uncertainties as a function of the corrected jet p_T in the central calorimeter ($0.2 < |\eta| < 0.6$).

between data and Monte Carlo in $\gamma + \text{jet}$ events. The systematic uncertainties from two other sources, the extra energy from multiple $p\bar{p}$ collisions and the underlying event, the energy associated with the spectator partons in a hard collision event, are negligible for this analysis.

In summary, the systematic uncertainties on jet energy measurements for jets in the central calorimeter ($0.2 < |\eta| < 0.6$) are shown in Fig. 4. The thick black line corresponds to the total uncertainty, obtained by adding in quadrature all the sources described above. Typically, it is 3% to 4% for jets with $p_T > 40 \text{ GeV}/c$. In order to check the energy corrections and systematic uncertainties, γ -jet events are used since the jet p_T range in this sample is similar to that in $t\bar{t}$ events. Figure 5 shows the difference between γ -jet balancing, defined as $p_T^{\text{jet}}/p_T^\gamma - 1$, in data and Monte Carlo after all jet corrections are applied. The $\pm 1\sigma$ range adequately covers the spread in these data points. These jet energy uncertainties are propagated to the top quark mass measurement as described in Sec. XII. Additional process-specific uncertainties are also considered in that section. The most important of these for the top quark mass measurement is the b -jet energy scale.

C. b -jet tagging using secondary vertex identification

The identification of b jets from top quark decay plays an important role in this analysis. Since most of the selected $W + \text{jets}$ events coming from non- $t\bar{t}$ processes do not contain bottom or charm quarks in the final state, requiring the presence of b jets provides significant background reduction.

The SECVTX silicon vertex b -jet tagging algorithm searches within a jet in the central region for a displaced secondary vertex due to the decay of a B hadron [44,45]. It uses tracks that are within $\Delta R < 0.4$ of the jet axis and

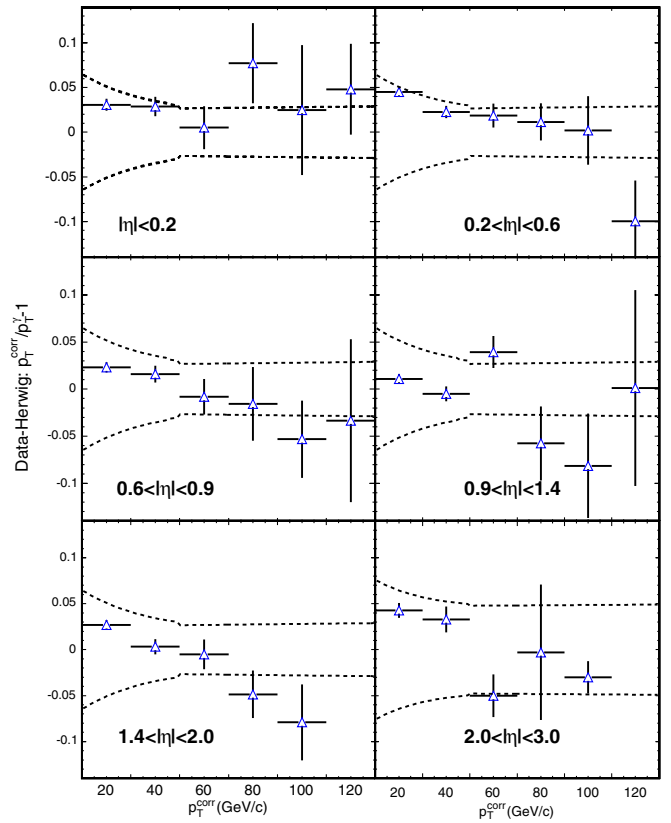


FIG. 5 (color online). The fractional difference between the jet and photon transverse momenta in γ -jet events are calculated after all jet corrections are applied. Plotted here is the difference between this quantity in data and simulation as a function of photon p_T , for different η ranges. The dashed lines show $\pm 1\sigma$ from the jet energy systematics.

have hits in the silicon detector. A set of cuts involving the transverse momentum, the number of hits, and the χ^2/ndf of the track fit are imposed to select good quality tracks in a jet. Then the algorithm is performed as follows: (1) Find at least three good tracks with $p_T > 0.5 \text{ GeV}/c$ and an impact parameter significance $|d_0/\sigma_{d_0}| > 2$, where d_0 is the impact parameter of the track relative to the accelerator beam line (measured on average for each store of $p\bar{p}$ collisions) and σ_{d_0} is the uncertainty coming from both the track and beam-line positions. At least one of the tracks must have $p_T > 1 \text{ GeV}/c$. (2) Reconstruct a secondary vertex using the selected tracks. (3) Calculate the two-dimensional decay length of the secondary vertex (L_{2D}) from the primary vertex. (4) Require $L_{2D}/\sigma_{L_{2D}} > 7.5$, where $\sigma_{L_{2D}}$ is the estimated uncertainty on L_{2D} , typically $190 \mu\text{m}$, to reduce the background from false secondary vertices (mistags). If a secondary vertex is not found, a second pass of the algorithm is carried out with tighter track requirements, demanding at least two tracks with $p_T > 1 \text{ GeV}/c$ and $|d_0/\sigma_{d_0}| > 3.5$, including at least one track with $p_T > 1.5 \text{ GeV}/c$. The cut on $L_{2D}/\sigma_{L_{2D}}$ is the same as in the first pass.

Based on simulation of the b -tagging algorithm, requiring at least one b -tagged jet keeps 60% of top quark events while removing more than 90% of background events. The difference between the efficiency in the simulation and that in the data is measured using a b -enriched dijet sample in which a nonisolated electron is found in one jet. We find a data to Monte Carlo tagging efficiency scale factor of 0.91 ± 0.06 [45], which is used with the Monte Carlo in estimating the expected background (see Sec. V). The uncertainty includes both systematic and statistical contributions. The main cause of the scale factor being less than 1.0 is the difference in track resolution between the data and Monte Carlo simulation.

D. Missing transverse energy: \cancel{E}_T

The presence of neutrinos is inferred from transverse energy imbalance in the detector. The missing transverse energy is calculated as

$$\cancel{E}_T = -\sum_i E_T^i \vec{n}_i, \quad (1)$$

where E_T^i is the magnitude of the transverse energy contained in calorimeter tower i , and \vec{n}_i is the unit vector from the interaction vertex to the tower in the plane transverse to the beam direction. If isolated high- p_T muon candidates are found in the event, the \cancel{E}_T is corrected by subtracting the energy deposited by the muon in the calorimeter, and adding the muon p_T to the vector sum. The typical \cancel{E}_T resolution in $t\bar{t}$ Monte Carlo events is approximately 20 GeV. Further corrections to \cancel{E}_T related to jet energy corrections and the transfer functions are described in Sec. VIII.

E. Event selection

The final state of the $t\bar{t}$ lepton + jets mode contains a high-momentum lepton candidate, missing transverse energy that indicates the presence of a neutrino from W leptonic decay, and four hadronic jets, of which two jets are expected to be b quarks. We summarize the selection criteria below.

Exactly one isolated electron (muon) candidate is required, having $E_T \geq 20$ GeV ($p_T \geq 20$ GeV/ c) and $|\eta| \leq 1.0$. Any event with two leptons satisfying the lepton criteria (see Sec. IVA) is removed. We also remove events where the second lepton candidate is an electron in the plug calorimeter or a muon that fails the CMUP requirement but has one CMU or CMP muon segment, to remove top dilepton events ($t\bar{t} \rightarrow l^+ \nu l^- \bar{\nu} b \bar{b}$). The missing transverse energy, \cancel{E}_T , is required to be greater than 20 GeV. Events with Z boson candidates are removed by requiring that there be no second object that forms an invariant mass with the primary lepton candidate within the window 76–106 GeV/ c^2 . Here, the second object is an oppositely signed isolated track with $p_T > 10$ GeV/ c for primary muons; for primary electrons it may be a track, an electro-

magnetic cluster, or a jet with $E_T > 15$ GeV and $|\eta| \leq 2.0$ that has fewer than 3 tracks and a high electromagnetic energy fraction. The primary vertex of the event must have its z coordinate within 60 cm of the center of the CDF II detector. The jets are clustered after removing towers within electron clusters and correcting each tower E_T for the location of the primary vertex z coordinate. We select the events that have exactly four jets with $E_T \geq 15$ GeV and $|\eta| \leq 2.0$ to better match the leading-order matrix element that is used in this analysis. This helps to reduce the contamination by initial and final-state radiation by 10% compared to events with four or more jets. Finally, at least one SECVTX tagged b jet is required. The above selection yields 63 b -tagged events in which 39 events contain an electron and 24 a muon. Of these 63, 16 double b -tagged events are observed. The overall selection efficiency for these criteria including the branching ratio, estimated from $t\bar{t}$ Monte Carlo simulation, is approximately $1.94\% \pm 0.01\%$ for the electron channel, $1.22\% \pm 0.01\%$ for muons in the CMUP, and $0.41\% \pm 0.01\%$ for muons in the CMX.

V. BACKGROUND ESTIMATE

It is important to this analysis that we have an accurate estimate of the background level in the final event sample because, to extract the top quark mass, we shift the measured mass to correct for background contamination (see Sec. IX B). We use the technique employed in the $t\bar{t}$ production cross-section measurements described in [44,45]. The major backgrounds come from misidentification, for example, a fake lepton and large missing E_T in events not containing a W boson, and events in which a light quark or gluon jet is mistagged as a b jet. The major physics background is the production of a W boson along with heavy flavor quarks.

A. Non- W (QCD) background

The non- W background (QCD multijets), events that do not contain a W boson, is estimated directly from the data, separately for electrons and muons. These events include fake leptons and missing energy as well as semileptonic B decays. An isolated primary lepton and large \cancel{E}_T due to the neutrino are characteristics of real W events, not shared by most non- W events. To estimate the number of non- W events in the sample, we use a 2-dimensional plot of \cancel{E}_T vs lepton isolation, defining four regions:

- (A) isolation > 0.2 and $\cancel{E}_T < 15$ GeV,
- (B) isolation < 0.1 and $\cancel{E}_T < 15$ GeV,
- (C) isolation > 0.2 and $\cancel{E}_T > 20$ GeV,
- (D) isolation < 0.1 and $\cancel{E}_T > 20$ GeV,

as shown in Fig. 6. Region D contains the real W events. For the non- W background, these two variables are assumed to be uncorrelated; therefore N_B/N_A , the ratio of the numbers of low \cancel{E}_T events at low and high isolation, is the same as N_D/N_C , the ratio at high \cancel{E}_T . The amount of

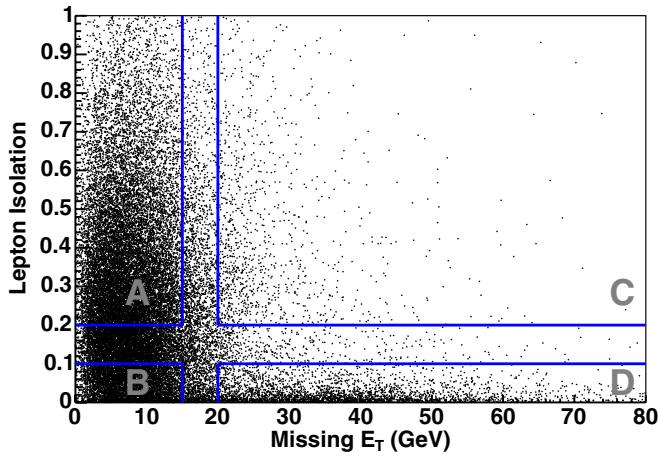


FIG. 6 (color online). Plot of missing E_T vs lepton isolation for events that contain an electron candidate (without an isolation cut) and two or more jets with $E_T > 15$ GeV and $|\eta| \leq 2.0$ before the b -tagging requirement is applied.

non- W contamination in region D is then calculated as $N_D(\text{non-}W) = (N_B \times N_C)/N_A$. Since backgrounds from W + heavy flavor ($Wb\bar{b}$, $Wc\bar{c}$, and Wc) and W + a mistagged jet are estimated by normalizing to the number of the “pretagged” events, those found prior to applying the b -tagging algorithm (see Sec. V C), the contributions of non- W background to both the pretagged and the tagged samples have to be measured, even though we use only the tagged sample estimate directly in the mass measurement. To evaluate the expected number of events in the tagged sample, we use two methods. One is to estimate N_D directly from the tagged sample. However, this is limited by low statistics, hence we lower the isolation boundary from 0.2 to 0.1 for regions A and C. A second method is to scale the estimate in the pretagged sample by the tagging rate for non- W events. The number of events in region B with 2 or more jets is used to obtain a reliable tag rate [45]. These two estimates are found to be consistent within the statistical uncertainty. The final estimate is obtained from the weighted average of the two methods.

B. Mistags

A SECVTX tag in a jet without a heavy flavor quark is called a “mistag.” The mistag rate per jet is measured using a large inclusive-jet data sample, without relying on the detector simulation. It is parametrized as a function of the number of tracks in the jet, the jet E_T before energy corrections, the η and ϕ of the jet, and the sum of the E_T 's of all jets in the event with $E_T > 10$ GeV and $|\eta| < 2.4$. To estimate the size of the mistag background, each jet in the pretag sample is weighted by its mistag rate, and then the sum of the weights over all jets in the sample is computed, after correcting for the fraction of pretagged events that are due to non- W background ($\sim 10\%$ for the electron and

$\sim 5\%$ for the muon channel) to avoid double counting these two background sources. Using the number of mistagged jets as the number of mistagged events is a good approximation because the mistag rate per jet is sufficiently low, typically 1%. This method is tested using samples of pure mistagged jets in which the jet and reconstructed secondary vertex are on opposite sides of the primary vertex. We find good agreement between the predicted and observed numbers of jets in the pretagged sample as a function of jet E_T [45].

C. W + heavy flavor (W + HF) backgrounds

The production of W bosons accompanied by QCD production of heavy flavor quarks in the processes $Wb\bar{b}$, $Wc\bar{c}$, and Wc produces a signature very similar to $t\bar{t}$ events in the final state, and is a significant part of the background for the tagged sample. These contributions, N_{HF} , are evaluated by $N_{\text{HF}} = N_{\text{pretag}} \times f_{\text{HF}} \times \epsilon_{\text{btag}}$, where N_{pretag} is the number of pretagged events in the data, f_{HF} is the fraction of pretagged events containing $Wb\bar{b}$, $Wc\bar{c}$, and Wc , estimated using the Monte Carlo models ALPGEN + HERWIG, and ϵ_{btag} is the b -tagging efficiency of each background source. The heavy flavor fractions are found to be approximately 2%–3% for $Wb\bar{b}$ and $Wc\bar{c}$, and 6% for Wc events, and were calibrated by comparing dijet Monte Carlo events with data. Details of these calculations can be found in [45].

D. Other backgrounds

The WW , WZ , and ZZ background, $Z \rightarrow \tau\tau$, and electroweak single top production by both s -channel $q\bar{q}$ fusion and t -channel W -gluon fusion processes are evaluated based on predictions from Monte Carlo simulation by multiplying the acceptances for these processes, as determined from the PYTHIA Monte Carlo program, by their production cross sections [46,47] and the integrated luminosity for the data sample. The Monte Carlo acceptance is corrected for the differences between Monte Carlo and data for lepton identification and trigger efficiencies. The b -tagging efficiency is also scaled by the MC/data tagging scale factor which was described in Sec. IV C.

E. Background summary

Events having a leptonic W decay plus 1 or 2 jets are used to test the background estimation procedure. We find agreement between the data and Monte Carlo predictions within their uncertainties. The results provide confidence that we can estimate the number of background events in the four-jet topology. The background contributions to the W + 4 jets sample are summarized in Table I. We estimate the total number of background events to be 9.2 ± 1.8 . The expected number of signal events for the predicted $t\bar{t}$ cross section ranges from 46 ± 5 events for $M_{\text{top}} = 170$ GeV/ c^2 (7.8 pb) to 37 ± 4 events for $M_{\text{top}} = 178$ GeV/ c^2 (6.1 pb).

TABLE I. The expected number of background events from individual sources and the fractions with respect to the 63 observed events.

Source	Number of events	Fraction (%)
Non- W (QCD)	3.07 ± 1.06	4.87
Mistag	2.27 ± 0.45	3.60
$Wb\bar{b}$	1.70 ± 0.79	2.70
$Wc\bar{c}$	0.81 ± 0.40	1.28
Wc	0.51 ± 0.23	0.81
$WW/WZ/ZZ$	0.39 ± 0.08	0.62
Single top	0.41 ± 0.09	0.65
Background total	9.2 ± 1.8	14.5
Observed events	63	100

The relative uncertainty on each cross-section value is roughly 10%, mainly coming from the parton distribution functions [48]. However, the estimate of 9.2 background events has been extracted with little dependence on the theoretical prediction of the $t\bar{t}$ cross section. We find that a 5 GeV/ c^2 difference in M_{top} (corresponding to about a 1.0 pb difference in the $t\bar{t}$ cross section) alters the background estimate by roughly 1%, corresponding to a negligible ~ 0.1 event. Therefore, in this analysis, 53.8 events are assumed to be from signal $t\bar{t}$ events (9.2 background events subtracted from the observed 63 events). This is supported by the 16 double b -tagged events in the data, where the expected number of events estimated by scaling the 63 observed events is 16.8 ± 1.8 events, including an expected 1.4 background events. For a kinematic comparison, the H_T distribution is shown in Fig. 7. H_T is defined as the scalar sum of the lepton E_T , the \cancel{E}_T and the E_T 's of the leading four jets. We find good agreement between the data and the Monte Carlo for both the double b -tag ratio and the kinematic distribution.

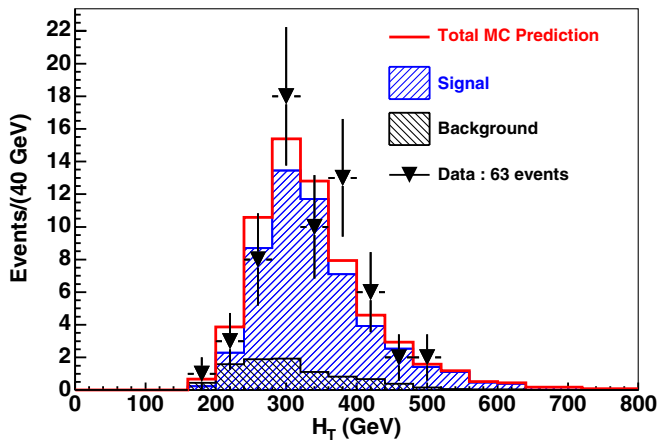


FIG. 7 (color online). H_T distribution for signal ($M_{\text{top}} = 178 \text{ GeV}/c^2$) and background, normalized to 53.8 and 9.2 events, respectively. The total 63 data events are shown as the triangles.

VI. ANALYSIS OVERVIEW

The analysis proceeds as follows. For each event, a likelihood as a function of top quark mass is calculated by the dynamical likelihood method (DLM), described in Sec. VII. The DLM defines a likelihood for each event based on the differential cross section per unit phase space of the final partons in the elementary process. It does not however use the number of observed events to constrain M_{top} based on the theoretical $t\bar{t}$ cross section. To infer the parton momenta, we employ transfer functions that relate the observed jet energies to the corresponding parton energies: four jets to four quarks ($q\bar{q}'$ from the W , b , and \bar{b}). The transfer functions are obtained from HERWIG Monte Carlo $t\bar{t}$ signal samples. Section VIII describes the details and performance checks of the transfer functions. There are 6 or 2 possible assignments of the four jets to the individual partons, depending on whether 1 or 2 jets are b -tagged, and for each assignment there are 2 solutions for the z component of the neutrino momentum. Instead of selecting one particular assignment (e.g., the one giving the maximum likelihood), we average the likelihoods for all possible jet assignments and neutrino solutions in an event, and such event likelihoods are multiplied together to obtain the joint likelihood function for the entire data sample. We take the average rather than the sum in order not to give greater weight to single b -tag events with their larger number of jet assignments. After calculating the top quark mass under the assumption that all events are $t\bar{t}$, the effect of the background is corrected by using a mapping function that provides a mass-dependent correction factor. The mapping functions are extracted using Monte Carlo pseudoexperiments in which the numbers of signal and background events are Poisson distributed around the expected means. The mean number of signal events is not changed for different top quark mass samples. Finally, we extract the measured value of the top quark mass using the expected background fraction estimated in Sec. V.

VII. DYNAMICAL LIKELIHOOD METHOD

The DLM was originally proposed in 1988 [10] and developed in [11,12]; details of the latest formulation are described in [13]. In DLM, we generate the parton kinematics from the observed quantities, and the likelihood of the reconstructed parton state is defined by the differential cross section per unit phase space of the final partons in the elementary process.

A. Definition of the likelihood

1. Differential cross section

The elementary parton process in a $p\bar{p}$ collision can be written as

$$a_1/p + a_2/\bar{p} \rightarrow \cdots \rightarrow C, \quad C \equiv \sum_{i=1}^n c_i, \quad (2)$$

where a_1 and a_2 are the initial partons—quark, antiquark, or gluon—in the proton and antiproton, respectively, and c_1, c_2, \dots, c_n are final-state partons and leptons. These are defined after initial-state radiation but before final-state radiation. In the case of the $t\bar{t}$ lepton + jets channel, the initial parton set (a_1, a_2) is (q, \bar{q}) , (\bar{q}, q) , or (g, g) , and the final leptons and partons are $l, \nu, q, \bar{q}', b, \bar{b}$, or their antiparticles, where (q, \bar{q}') are quarks from W decay, and $l = e$ or μ . Throughout this paper, a particle 4-momentum and its 3-momentum are represented by a small letter in italics and in bold, respectively: e.g., a symbol “ p ” represents the proton’s 4-momentum, and \mathbf{p} its 3-momentum. The final partons are assumed to have their pole masses (4.8 GeV/ c^2 for the b jets and 0.5 GeV/ c^2 for the W daughter jets), so that their 3-momenta define their states unambiguously.

The hadronic cross-section for process (2) is given by

$$d\sigma = dz_{a_1} dz_{a_2} d^2\mathbf{p}_T f_{a_1/p}(z_{a_1}) f_{a_2/\bar{p}}(z_{a_2}) \times f_T(p_T) d\hat{\sigma}(a_1 + a_2 \rightarrow C; \boldsymbol{\alpha}), \quad (3)$$

where $d\hat{\sigma}$ is the parton level cross section [49],

$$d\hat{\sigma}(a_1 + a_2 \rightarrow C; \boldsymbol{\alpha}) = \frac{(2\pi)^4 \delta^4(a_1 + a_2 - C)}{4\sqrt{(a_1 \cdot a_2)^2 - m_{a_1}^2 m_{a_2}^2}} \times |\mathcal{M}(a_1 + a_2 \rightarrow C; \boldsymbol{\alpha})|^2 \times d\Phi_n^{(f)}(a_1 + a_2; C). \quad (4)$$

In Eq. (3), the symbol $\boldsymbol{\alpha}$ represents a set of dynamical constants to be measured, e.g., masses, decay widths, and coupling constant ratios. In this analysis, $\boldsymbol{\alpha}$ is simply the top quark mass M_{top} . The variables z_{a_1} and z_{a_2} are the energy fractions of a_1 and a_2 in hadrons p and \bar{p} , respectively, and m_{a_1} and m_{a_2} are their masses that are assumed to be zero in this analysis. \mathbf{p}_T is the total transverse momentum of the initial and final systems in the plane transverse to the beam axis. Functions $f_{a_1/p}(z_{a_1})$ and $f_{a_2/\bar{p}}(z_{a_2})$ denote the parton distribution functions (PDF’s), while $f_T(p_T)$ is the probability density function for the total transverse momentum of the system acquired by initial-state radiation. In this analysis, we use the leading-order PDF, CTEQ5L [34]. Other PDF sets are used to calculate the systematic uncertainty. The function $f_T(p_T)$ is obtained by running the PYTHIA generator.

In Eq. (4), \mathcal{M} is the matrix element of the process that is being studied (in this case, $t\bar{t}$ production and decay described in Sec. VII B), and $d\Phi_n^{(f)}$ is the Lorentz invariant phase space element,

$$d\Phi_n^{(f)} = \prod_{i=1}^n \frac{d^3\mathbf{c}_i}{(2\pi)^3 2E_i}. \quad (5)$$

We use Eq. (4) to formulate the parton level likelihood. The basic postulate is that final partons occupy an n -dimensional unit phase space volume in the neighbor-

hood of $\mathbf{c} = (c_1, \dots, c_n)$. When a momentum set \mathbf{c} is given, the total probability for this final state to occur is obtained by integrating Eq. (3) over initial-state variables z_{a_1}, z_{a_2} , and \mathbf{p}_T , as

$$\frac{d\sigma}{d\Phi_n^{(f)}} = I(a_1, a_2) |\mathcal{M}(a_1 + a_2 \rightarrow C; \boldsymbol{\alpha})|^2, \quad (6)$$

where

$$I(a_1, a_2) = \frac{(2\pi)^4}{4\sqrt{(a_1 \cdot a_2)^2}} f_{a_1/p}(z_{a_1}) f_{a_2/\bar{p}}(z_{a_2}) f_T(p_T) \quad (7)$$

is the integration factor for the initial state. Because of the δ function in Eq. (4), the initial parton momenta a_1 and a_2 are uniquely defined by that of C .

For a given set of $\mathbf{c} = (c_1, \dots, c_n)$, we define the parton level likelihood for $\boldsymbol{\alpha}$ by

$$L_1^{(p)}(\boldsymbol{\alpha}|\mathbf{c}) = l_0 \frac{d\sigma}{d\Phi_n^{(f)}}, \quad (8)$$

where l_0 is given by

$$l_0 = \frac{1}{\epsilon(M_0) \sigma_T(M_0)}. \quad (9)$$

In Eq. (9), $\sigma_T(M_0)$ and $\epsilon(M_0)$ are the total cross section and the detection efficiency for the true (pole) top quark mass of the sample, respectively. Thus l_0 is the integrated luminosity per event in the sample. This method does not make use of any constraint from the theoretical $t\bar{t}$ cross section as a function of M_{top} . Since l_0 only depends on the true (pole) top mass, it does not vary event by event in the sample [13] and only changes the absolute value of the likelihood, i.e., it has no effect on the final result. In this sense, this is not a real likelihood and any bias has to be corrected by the mapping function. The statistical uncertainty is also corrected by checking the pull distribution as described in Sec. IX.

2. Propagator factors

When process (2) includes internal lines of the Feynman graph, for example r in

$$a_1/p + a_2/\bar{p} \rightarrow r + c_{j+1} + \dots + c_n, \quad (10)$$

$$r \rightarrow c_1 + \dots + c_j, \quad (11)$$

we have to consider the propagator factor for a particle r . We treat, in this channel, t, \bar{t}, W^+ , and W^- as internal lines (r) as illustrated in Fig. 1.

We factorize the matrix element as

$$|\mathcal{M}(a_1 + a_2 \rightarrow C; \boldsymbol{\alpha})|^2 = |\mathcal{M}_{\text{prod}}|^2 \mathcal{P}(s_r) |\mathcal{M}_{\text{dec}}|^2, \quad (12)$$

where $\mathcal{M}_{\text{prod}}$ and \mathcal{M}_{dec} are the matrix elements for the production process and decay, respectively, and s_r is the virtual mass squared of r , which satisfies

$$s_r = \left(\sum_{i=1}^j c_i \right)^2. \quad (13)$$

For the propagator factor $\mathcal{P}(s_r)$, we assume the Breit-Wigner form,

$$\mathcal{P}(s_r) = \frac{1}{(s_r - M_r^2)^2 + M_r^2 \Gamma_r^2}. \quad (14)$$

In the reconstruction of ν_z , the unmeasured z component of the neutrino momentum, we generate the W mass squared s_W according to $\Pi(s_W)$, where

$$\Pi(s) = \mathcal{P}(s) / \int \mathcal{P}(s) ds, \quad (15)$$

and solve Eq. (13) for ν_z (quadratically ambiguous). The function $\Pi(s)$ satisfies

$$\int_0^\infty \Pi(s) ds = 1. \quad (16)$$

3. Transfer functions for observables

Final quarks and gluons are not directly observed; they undergo hadronization, are observed by detectors with finite resolution, and are reconstructed as jets. Jet energies are generally calibrated using generic QCD jets, so we need additional corrections for b jets and W daughter jets in the $t\bar{t}$ processes. To describe the relation between the parton and observed quantities (observables), we introduce the transfer function (TF) $w(\mathbf{y}|\mathbf{x})$, where \mathbf{y} represents a set of observables and \mathbf{x} is a parton variable set that corresponds to \mathbf{y} . In the $l +$ jets process, \mathbf{y} consists of the momenta of the e or μ and of the 4 jets, and the missing transverse energy (\cancel{E}_T). In the present analysis, we use the TF only for quarks and jets. Electrons and muons are measured well in the detector, and \cancel{E}_T is calculated from other observed quantities in an event (see Sec. VIII B).

The differential probability for the parton variables \mathbf{x} to be observed as \mathbf{y} , $dP(\mathbf{y}; \mathbf{x})$, is defined by the TF $w(\mathbf{y}|\mathbf{x})$ as

$$dP(\mathbf{y}; \mathbf{x}) = w(\mathbf{y}|\mathbf{x}) d\mathbf{y}. \quad (17)$$

The TF for a single quark, $w(\mathbf{y}|\mathbf{x})$, is obtained from the (x, y) distribution of the $t\bar{t}$ Monte Carlo events. The event selection criteria are applied to these events. The effect of the detection efficiency for the variable set (x, y) is thus included in the determination of $w(\mathbf{y}|\mathbf{x})$, and the normalization condition,

$$\int w(\mathbf{y}|\mathbf{x}) d\mathbf{y} = 1, \quad (18)$$

holds.

4. Likelihood for a single path, a single event, and multiple events

Single path reconstruction and its likelihood.—The single path likelihood is defined for each complete set of parton kinematics and calculated as follows:

- (1) We assume that the momentum of the e or μ is precisely measured.
- (2) The four jets are assigned to the four final-state quarks. We call such an assignment a “topology” denoted by I_t ($I_t = 1, \dots, N_t$). Therefore N_t represents 6 or 2 possible topologies in an event, depending on whether 1 or 2 jets are b -tagged.
- (3) Once a topology is specified, we randomly generate the parton kinematics $(b, \bar{b}, q, \bar{q}')$ according to the transfer functions. We identify the momentum direction of each jet with that of the assigned quark, and transfer variables \mathbf{x} ($E_{Tb}, E_{T\bar{b}}, E_{Tq}, E_{T\bar{q}'}$) are chosen using as input \mathbf{y} , the transverse energies of the corresponding jets. More details are given in Sec. VIII. Each random generation is denoted by k .
- (4) After (1), (2), and (3), the transverse momentum of the neutrino (ν_x, ν_y) is identified with the measured value of \cancel{E}_T and then corrected using both jet corrections and (k th) jet transfer functions. Details of this correction are discussed in Sec. VIII. Then the parton momenta are defined except for ν_z , the unmeasured z component of the neutrino momentum. To get ν_z we choose s_W according to $\Pi(s_W)$ in Eq. (15), and ν_z is obtained by solving Eq. (13). A quadratic ambiguity results in two solutions (ν_{z1}, ν_{z2}) that are specified by an integer I_s ($= 1$ or 2), which is treated separately from topology as defined in (2).
- (5) From procedures (1), (2), (3), and (4), an event configuration (I_t and I_s) and parton momenta (k for a generation by the transfer functions) are uniquely specified. The likelihood of a single path is then

$$L_1^{(k)}(I_t, I_s, \mathbf{x}_k; M_{\text{top}} | \mathbf{y}^{(i)}) = l_0 \frac{d\sigma}{d\Phi_6^{(f)}} \times (I_t, I_s, k, i; M_{\text{top}}), \quad (19)$$

where i is the event number, and $d\Phi_6^{(f)}$ is the phase space for $(l, \nu, b, \bar{b}, q, \bar{q}')$. In this context, when we use a “single path” the likelihood (the differential cross section) can be calculated without any ambiguity, since all information such as assignments and parton momenta are determined. Then, for each path, we make a parameter scan of M_{top} uniformly in its search region (typically 155–195 GeV/ c^2).

Likelihood for a single event.—All possible paths (configurations), each labeled by k, I_t , and I_s , are mutually exclusive, and we define the likelihood of the i th event as

the average of the likelihoods for all paths,

$$L(M_{\text{top}}|\mathbf{y}^{(i)}) = \frac{l_0}{2KN_t} \sum_{k=1}^K \sum_{I_t=1}^{N_t} \sum_{I_s=1}^2 L_1^{(k)}(I_t, I_s, \mathbf{x}_k; M_{\text{top}}|\mathbf{y}^{(i)}). \quad (20)$$

This definition of the event likelihood thus contains the correct set of (I_t, I_s) (if the event is $t\bar{t} \rightarrow l + \text{jets}$). The sum over k corresponds to the numerical integration of the parton kinematics according to the transfer functions. Therefore we repeat the procedures (2)–(5) a large enough number of times (K) so that the value of $L(M_{\text{top}}|\mathbf{y}^{(i)})$ converges, which is typically 50 000 times. In summary, each time a parton configuration and set of momenta are selected (I_t, I_s , and k), we calculate the likelihood (single path) and in order to obtain the event likelihood, we average all possible single path likelihoods by numerical integration.

Likelihood for multiple events.—The single event likelihood is a function of M_{top} . For multiple events, we get mutually independent functions of M_{top} . Hence, to obtain the top quark mass from a total of N_{ev} events, we form the product of all the event likelihoods, and take negative 2 times the logarithm of this product,

$$(M_{\text{top}}) = -2 \ln \left(\prod_{i=1}^{N_{\text{ev}}} L(M_{\text{top}}|\mathbf{y}^{(i)}) \right). \quad (21)$$

Then we obtain the top quark mass as the maximum likelihood estimate of M_{top} ,

$$\hat{M}_{\text{top}} = M_{\text{top}} \text{ at the minimum of } \Lambda(M_{\text{top}}), \quad (22)$$

and its uncertainty from the points where $\Delta\Lambda = 1$.

B. Matrix element calculation in the lepton + jets channel

The matrix element squared $|\mathcal{M}|^2$ is factorized into 3 parts: (1) $t\bar{t}$ production ($|\mathcal{M}_{t\bar{t}}|^2$), (2) the propagators of the top and antitop (\mathcal{P}_{tl} and \mathcal{P}_{th}), and (3) the decay matrices, $|\mathcal{M}_{tl}|^2$ and $|\mathcal{M}_{th}|^2$, for leptonic and hadronic top decays, respectively. Namely,

$$|\mathcal{M}|^2 = |\mathcal{M}_{t\bar{t}}|^2 \mathcal{P}_{tl} \mathcal{P}_{th} |\mathcal{M}_{tl}|^2 |\mathcal{M}_{th}|^2. \quad (23)$$

The production matrix element for the $q\bar{q}$ initial state at leading order [50–52] is

$$|\mathcal{M}_{t\bar{t}}(q\bar{q} \rightarrow t\bar{t})|^2 = \frac{2g_s^4}{9} (2 - \beta^2 \sin^2 \theta^*), \quad (24)$$

where θ^* is the angle between the top quark and the incident quark in the proton in the $t\bar{t}$ center-of-mass system, β is the velocity of the top quark, and g_s is the strong coupling constant.

For the gg initial state [50–52], the matrix element can be expressed as

$$|\mathcal{M}_{t\bar{t}}(gg \rightarrow t\bar{t})|^2 = g_s^4 \left(\frac{1}{6\tau_1\tau_2} - \frac{3}{8} \right) \left(\tau_1^2 + \tau_2^2 + \rho - \frac{\rho^2}{4\tau_1\tau_2} \right), \quad (25)$$

where

$$\begin{aligned} \tau_1 &= \frac{2(g_1 \cdot t)}{\hat{s}}, & \tau_2 &= \frac{2(g_2 \cdot t)}{\hat{s}}, \\ \rho &= \frac{4M_{\text{top}}^2}{\hat{s}}, & \hat{s} &= (g_1 + g_2)^2, \end{aligned} \quad (26)$$

g_1 and g_2 are the incident gluon momenta in the proton and antiproton, and M_{top} is a free parameter for the top quark mass. In these equations, the $t\bar{t}$ spin correlations have been ignored. This effect is included in the mapping functions described in Sec. IX B since spin correlations are included in the HERWIG Monte Carlo samples that are used to make the mapping functions. Since we do not know what the initial state was, the likelihoods for the two processes ($q\bar{q}$ and gg) are summed up in the event likelihood with the appropriate PDF weights obtained from CTEQ5L.

The propagators for the top and antitop quarks are as specified by Eq. (14) in which M_r corresponds to M_{top} and s_r is the invariant mass of the leptonically (tl) or hadronically decaying top quark (th).

The decay matrix elements for the leptonic and hadronic channels are given by

$$|\mathcal{M}_{tl}|^2 = 4g_w^4 \frac{(t \cdot l)(b \cdot \nu)}{(S_{l\nu} - M_W^2)^2 + M_W^2 \Gamma_W^2}, \quad (27)$$

$$|\mathcal{M}_{th}|^2 = 4g_w^4 \frac{1}{2} \sum_{i \leftrightarrow j} \frac{(\bar{t} \cdot q_i)(\bar{b} \cdot q_j)}{(S_{2j} - M_W^2)^2 + M_W^2 \Gamma_W^2}, \quad (28)$$

where $S_{l\nu}$ and S_{2j} represent the invariant masses squared of the lepton + neutrino and the two quarks from the W , respectively. For the mass and decay width of the W , we assume the world average values, $M_W = 80.4 \text{ GeV}/c^2$ and $\Gamma_W = 2.1 \text{ GeV}/c^2$. In Eq. (27), the dot product of b and ν can be calculated because the z component of the neutrino momentum, ν_z , has already been determined in step (4) above. In Eq. (28), we make both possible assignments of the two jets to q and \bar{q}' from the W , and the likelihoods corresponding to the two possibilities are averaged.

VIII. TRANSFER FUNCTIONS (TF)

As described in the preceding section, the transfer functions deal with the relation between parton and corrected jet energies. This allows us to use the full distribution, including tails, of the fraction of quark energy deposited outside of the jet cone. Also, since the generic jet corrections are based on the QCD dijet process, the transfer functions can correct for $t\bar{t}$ -specific b jets and W daughter jets.

A. Definition and performance

The transfer variable set (x, y) we use in this analysis is the transverse energy of a parton (quark) and the corresponding jet,

$$x = E_T(\text{parton}), \quad y = E_T(\text{jet}), \quad (29)$$

where $E_T(\text{jet})$ has been corrected with the CDF generic corrections described in Sec. IV B 1. TF's are obtained for b jets and W daughter jets separately and are applied only to the four highest E_T jets in an event, which are assumed to come from the t and \bar{t} decay.

The TF's are obtained with the following procedure. We generate events with the HERWIG and PYTHIA Monte Carlo event generators and a full detector simulation, and select events with the same criteria as applied to real data. From the accepted events, we select those jets that are within a distance $\Delta R < 0.4$ from a final-state quark. Using these "matched" jets, we obtain a 2-dimensional density function of the number of events at (x, y) , $D(x, y; M_{\text{top}})$.

The number of events in a $dx dy$ bin is given by

$$D(x, y; M_{\text{top}})dx dy = L_{\text{int}} \left(\frac{d\sigma}{dx} \right) dx \times w(y|x|M_{\text{top}}) dy \quad (30)$$

where L_{int} is the integrated luminosity of the sample. The transfer function is obtained by removing the cross-section factor from $D(x, y; M_{\text{top}})$, i.e.,

$$w(y|x|M_{\text{top}}) = \frac{1}{n_x} D(x, y; M_{\text{top}}), \quad (31)$$

where

$$n_x = L_{\text{int}} \frac{d\sigma}{dx} = \int D(x, y; M_{\text{top}}) dy. \quad (32)$$

Values of n_x and $w(y|x|M_{\text{top}})$ are numerically obtained from $D(x, y; M_{\text{top}})$ by Eqs. (31) and (32), respectively.

The TF $w(y|x|M_{\text{top}})$ depends on M_{top} , most significantly through the event selection criteria. The total selection efficiency is about 2%–3% depending on an input M_{top} ; approximately 4000 events are accepted from the 200 000 events, which is the typical size of the Monte Carlo sample for each top quark mass point. Thus the statistics of the Monte Carlo samples are not sufficient to obtain an M_{top} -dependent TF. Therefore, as an approximation, we use TF's averaged over the M_{top} search region (130–230 GeV/ c^2 , sampled every 5 GeV/ c^2),

$$w(y|x) = \langle w(y|x|M_{\text{top}}) \rangle_{M_{\text{top}}}. \quad (33)$$

The transfer variables x and y are strongly correlated, so we make a variable transformation from (x, y) to (ξ, Y) as

$$\xi = \frac{x - y}{x}, \quad Y = y. \quad (34)$$

The TF for variables (ξ, Y) is defined by

$$f(\xi, Y) d\xi dY = \frac{1}{n_x} D(x, y) dx dy. \quad (35)$$

In practice, $f(\xi, Y)$ is obtained by filling a (ξ, Y) histogram with weight $1/n_x$ for each Monte Carlo event. We call the variable ξ a "response variable" in this paper. In the function $f(\xi, Y)$, ξ and Y are much less correlated than x and y in $w(y|x)$, so wider bins can be used in Y . In the reconstruction of parton kinematics, ξ is generated from the observed value of $Y(= y)$ according to $f(\xi, Y)$, and x is then determined by Eq. (34).

An advantage of deriving the TF from Monte Carlo events is that the effect of the detection efficiency and acceptance is automatically included in the determination of the TF.

As illustrated in Fig. 8, the TF's strongly depend on the E_T and slightly depend on pseudorapidity η of the jets. Therefore we calculate TF's in 10 bins of jet E_T (15 to >105 GeV in 10 GeV steps) and 3 bins of $|\eta|$ (0.0–0.2–0.6–2.0) that correspond to different regions of the calorimeter [22]. Thus, separately for b and W jets, we make 30 histograms. In each bin, the mass averaged TF contains 5000 jets on average, while if we use M_{top} -dependent TF, it is about 250 which is not enough to get smooth functions. In the figure, the means of the response variable as a function of E_T are compared with the transfer functions extracted from only a single mass sample ($M_{\text{top}} = 178 \text{ GeV}/c^2$). The b -jet response is lower (higher) at lower

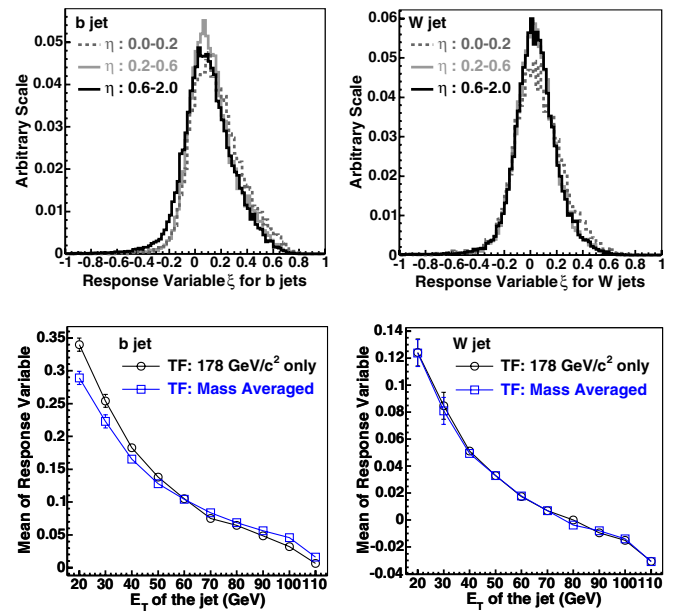


FIG. 8 (color online). The distributions of the response variable ξ for b jets (upper-left panel) and W jets (upper-right panel) for different ranges of jet η . Each distribution is normalized to the unit area. The jet E_T dependence is shown in the lower-left panel and lower-right panel for b and W jets, respectively, by plotting the mean of the response variables as a function of jet E_T .

(higher) E_T for the mass averaged TF, while for W jets the response is almost identical. This is because the b jets, being the direct daughters of the top quarks, carry more of the mass information. By averaging over the samples in a wide mass range, the top quark mass dependence is reduced without needing the enormous statistics for making mass-dependent TF's. The response distributions are asymmetric due to the finite size of the clustering cone. Consequently we do not fit the distributions with a functional form, but rather generate random numbers to accurately sample the full distributions.

To validate the transfer function performance using $t\bar{t}$ Monte Carlo samples with different masses, we investigate the invariant mass of the jet pair from the W and the three jets from the hadronically decaying top quark using the following procedure.

- (1) *Jet-parton matching.*—To ensure proper assignment of jets to partons, we require the distance (ΔR) between a jet's direction and a parton's direction to be less than 0.4. Moreover, if two or more jets are within $\Delta R < 0.4$ of a parton direction, we discard the event.
- (2) *Applying the transfer function.*—This is performed by random generation of the response variable ξ from the given $Y = y$. Explicitly, the transverse energy of the parton is obtained by

$$E_T(\text{parton}) = \frac{E_T(\text{jet})}{(1 - \xi)}. \quad (36)$$

Then the dijet (W) and trijet (top) invariant masses are calculated. The random number generation is repeated more than 50 000 times (we call this ‘‘scanning’’). After scanning, distributions of the dijet and trijet invariant masses are obtained for each event.

- (3) *Extracting the invariant mass.*—We calculate the mean of the distribution obtained in step 2 by fitting the distribution from each event with a Gaussian function and storing the fitted mean value in a histogram.

The invariant masses of the dijets and trijets before and after applying the transfer function are shown in Fig. 9. Since the out-of-cone correction is not applied to the masses before the transfer function (we start with hadrons within the jet cone and apply the transfer function to obtain the parton energy), lower masses are observed, while after the transfer function is applied, the final values of the mean agree with the generated input masses. The left plots in Fig. 10 show the η dependence of the invariant masses, while the right plots show the p_T dependence. There is a large p_T dependence in the plots before the transfer functions are applied. The transfer functions, however, largely eliminate this dependence.

We investigate the Monte Carlo generator dependence by comparing PYTHIA and HERWIG, which have different fragmentation modeling, but no significant discrepancies are observed. Since the top quark mass samples are pro-

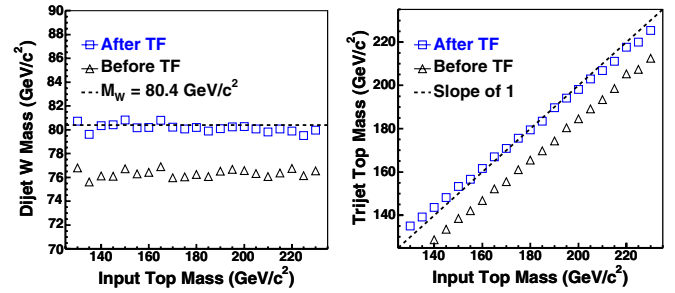


FIG. 9 (color online). Comparisons of reconstructed invariant masses of W dijets (left panel) and top trijets (right panel) in HERWIG Monte Carlo samples, as a function of input top quark mass, before and after the transfer function is applied. Dashed lines correspond to the input masses of the W and top quark.

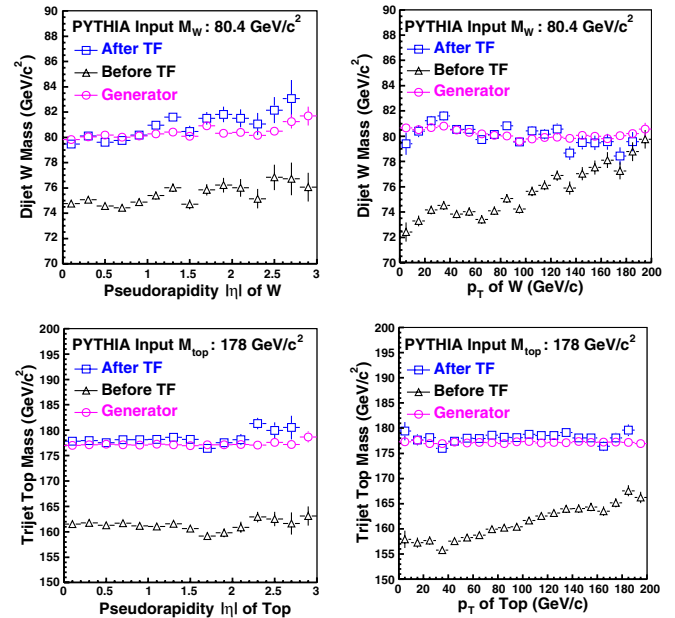


FIG. 10 (color online). η and p_T dependence of dijet W (upper panel) and trijet top (lower panel) invariant masses, with the generated masses in PYTHIA Monte Carlo shown as open circles. Masses with only generic corrections are shown in open triangles, and the open squares show the results after TF application.

duced with HERWIG, we make the transfer functions with HERWIG and examine the generator bias in Sec. XII. We also check alternative variables that could be used in the response function: jet E , p , or p_T . As with the generator dependence, no differences are found in the shape or mean of the response functions or in the reconstructed invariant masses of W dijets or top trijets.

B. Missing transverse energy

The ‘‘raw \cancel{E}_T ,’’ which is defined in Eq. (1), is corrected by applying generic jet energy corrections and then the transfer functions. First, the definition of missing trans-

verse energy is rewritten using the observed objects in the sample to take into account the generic jet corrections,

$$-\cancel{E}_T = E_T(\text{lepton}) + \sum_{i=1}^4 E_T^i(\text{jet}) + X_T, \quad (37)$$

where $E_T^i(\text{jet})$ is the E_T of the jet after generic corrections, and X_T corresponds to all other calorimeter-deposited energies. (Within X_T , the generic corrections are also applied to all jets with $E_T > 8$ GeV and $|\eta| < 2.4$.) The above expression shows that the \cancel{E}_T measurement is highly correlated with the jet energy measurements and corrections. Therefore, it is not considered to be an independent observable in this analysis. We calculate the transverse component of the neutrino momentum, ν_T , from the leptonic W decay as

$$\nu_T = \cancel{E}_T + \sum_{j=1}^4 (E_T^j(\text{jet}) - E_T^j(\text{corr})) \quad (38)$$

where $E_T^j(\text{corr})$ is the jet E_T after generic and transfer function corrections are applied to each of the leading four jets.

IX. TOP QUARK MASS RECONSTRUCTION

This section describes how we extract the top quark mass and checks of the top quark mass reconstruction using Monte Carlo simulation. In this analysis, all events are assumed to be signal when the likelihood is calculated. The result is then corrected for the presence of background. Therefore, we first present the behavior of the background and its effects on signal reconstruction. Based on large sets of pseudoexperiments with varying background fractions, we derive the background correction function (“mapping function”) for the top quark mass parametrized as a function of the background fraction. At this point, this method is fully calibrated with the Monte Carlo sample.

A. Background effect on the likelihood

As described in Table I in Sec. V, there are various background processes that may affect this measurement. We use the ALPGEN Monte Carlo with the CDF detector simulation to model mistags and W + heavy flavor events. The W + four light-flavor partons ($W4p$) process can be used to investigate mistags, since mistags come from a false secondary vertex, which is mainly due to track and vertex resolution effects. For non- W (QCD) background, we use a nonisolated lepton sample (isolation $I > 0.2$, but $E_T > 20$ GeV) from real data. Other electroweak processes, diboson and single top production, are modeled by PYTHIA Monte Carlo samples. All events are subject to the event selection described in Sec. IV.

The likelihood distribution and the mass likelihood peak are expected to be changed by the existence of background

events. To understand the background effects more fully, we first calculate the dynamical likelihood defined by Eq. (20) for each background sample, and the average joint maximum likelihood masses are estimated from pseudoexperiments with ~ 100 – 1000 events, depending on the background source. Their values mainly result from the lepton ($E_T > 20$ GeV) and jet energy ($E_T > 15$ GeV) cut thresholds. The mistag, W + HF, and non- W samples produce almost the same maximum location in the range of 155 – 160 GeV/ c^2 , while the single top sample has 170 GeV/ c^2 , a slightly higher mass. The diboson background has a slightly lower mass, around 155 GeV/ c^2 , near the lower limit of the search region (155 – 195 GeV/ c^2). For each background, the peak width of maximum likelihood masses per event is much larger than for signal events, and its peak is relatively lower compared to the top quark mass search range (as shown in Fig. 22 in Sec. XI).

The effect of background on top quark mass extraction is seen in Fig. 11, which shows the reconstructed top quark mass from 63-event pseudoexperiments as a function of the background fraction. The peak mass is shifted lower and the width broadens as the background fraction increases.

It is important to know the effect of each of the backgrounds on the mass determination in order to properly account for the background composition uncertainty. Figure 12 shows, for 178 GeV/ c^2 $t\bar{t}$ Monte Carlo, how the reconstructed mass is shifted from the input mass by individual background sources as the background fraction is varied over the range 0% – 50% . This is done with pseudoexperiments having 63 total events, where the number of background events is fluctuated using Poisson statistics. We do not see significant differences among the

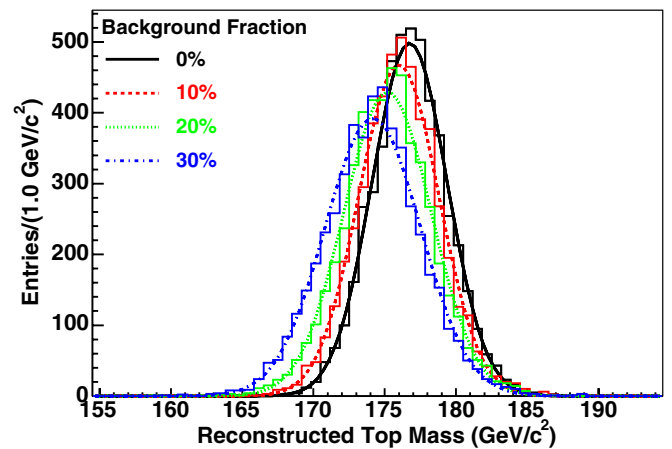


FIG. 11 (color online). An example of mass shift due to background events. The plot shows the reconstructed mass (input $M_{\text{top}} = 178$ GeV/ c^2), varying the background fraction from 0% to 30% (expected fraction is 14.5%). For each distribution, 5000 sets of pseudoexperiments that contain 63 events each are performed. Each distribution is fitted with a Gaussian function.

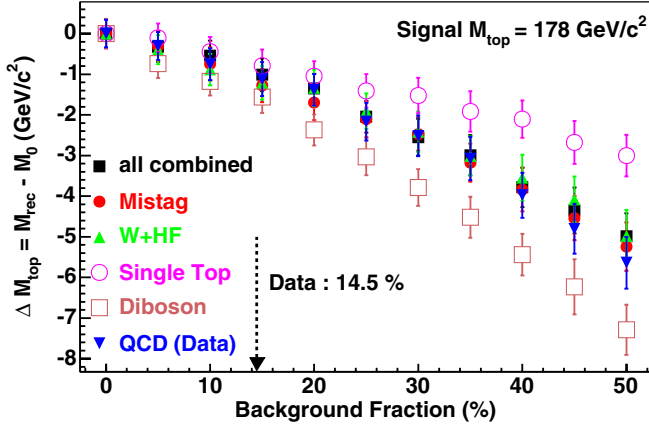


FIG. 12 (color online). The difference between the reconstructed mass (M_{rec}) and M_0 , the mass at 0% background ($\sim 177.5 \text{ GeV}/c^2$), due to individual background sources, using a signal sample of $M_{\text{top}} = 178 \text{ GeV}/c^2$, as a function of the background fraction. The closed squares represent the combined background using the expected composition from Table I. The expected background fraction of 14.5% is shown as the dashed line.

$W + \text{HF}$, mistag, and non- W (QCD) samples, which in sum account for more than 90% of the background and hence dominate the total background (the solid squares in Fig. 12). Thus the size of the mass shift produced by the background is not sensitive to the relative fractions of $W + \text{HF}$, mistag, and non- W . On the other hand, the single top sample produces a smaller negative shift and diboson events a slightly larger negative shift compared to the dominant sources of mistag/ $W + \text{HF}$ /non- W . Each of these two sources is responsible for approximately 5% of the total background.

In summary, background reduces the likelihood peak mass. We evaluate the size of these mass shifts and derive a correction, the “mapping function” discussed in the next section.

B. The mapping function

There are two sources that cause the input top quark mass and the reconstructed top quark mass to differ. One is the top quark mass dependence of the transfer function, and the other is the effect of background. We combine the two effects into a single mass-dependent correction factor, the mapping function, which is obtained from many sets of pseudoexperiments. Figure 13 shows the reconstructed top quark mass as a function of its input mass for various background fractions. The background fraction ranges from 0% to 50%, where the relative fraction of each background is that given in Table I. In each pseudoexperiment, the number of events from each background source and the total number of events are Poisson fluctuated. As one can see in the figure, even with 0% background the reconstructed top quark mass does not have unit slope. This

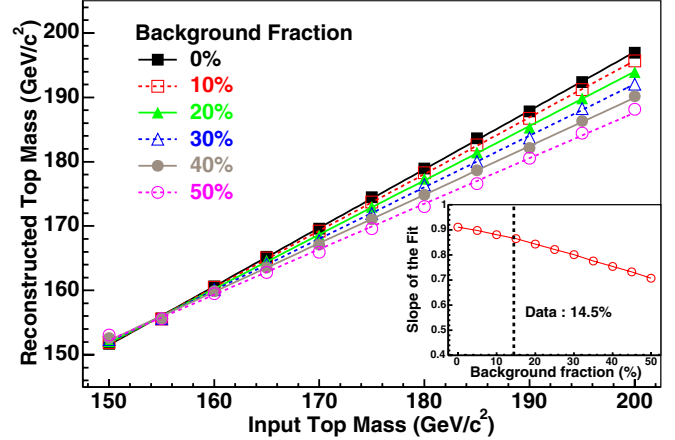


FIG. 13 (color online). The reconstructed mass obtained from the mean of the pseudoexperiments, as a function of input mass with the background fraction varying from 0% to 50%. The inset shows the slope of the linear fit to the mapping function as a function of the background fraction. The expected background fraction of 14.5% in this data sample is shown as the dashed line.

is due to a small top quark mass dependence of the transfer function as well as to the effect of gluon radiation and the contamination of the data sample from other top quark decay modes. As expected from the background study, the reconstructed top quark mass is shifted lower as the background fraction increases. The inset of Fig. 13 shows the slope of the linear fit (p_0 of $p_0 \cdot x + p_1$) to the mapping functions as a function of the background fraction. One can see very stable behavior up to a background fraction of 50%. The estimated background fraction of 14.5% is used to extract the top quark mass.

C. Method check

The method described above is tested for possible systematic bias by running large numbers of pseudoexperiments using Monte Carlo samples. Each set of 63 events (mean) in a pseudoexperiment consists of on average 53.8 signal events and 9.2 background events, with each source Poisson fluctuated. For each pseudoexperiment, the fit of the $-2 \ln L$ distribution provides a measured top quark mass as well as the positive and negative uncertainties by fitting with a second order polynomial with different curvature on the positive and negative sides (four parameters). After applying mapping functions for a 14.5% background fraction to each pseudoexperiment, we obtain a slope consistent with unity (0.997 ± 0.006) between the input and reconstructed masses. A pull distribution, defined as the input top quark mass minus the reconstructed mass divided by its estimated uncertainty, is generated for each of 11 different input top quark mass samples, where each mass point is generated from 1000 pseudoexperiments and then is fitted with a Gaussian function to extract the center and the width of the pull distribution. The center of the pull distribution is consistent with zero (0.015 ± 0.021) as

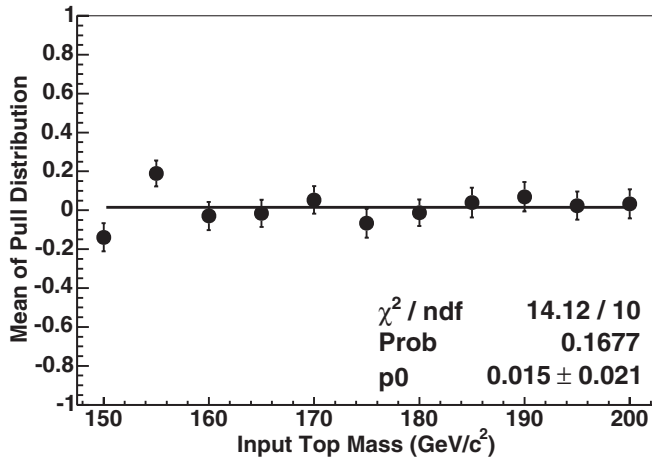


FIG. 14. The mean (center) of the pull distribution as a function of the input top quark mass is consistent with zero, as shown in the figure.

illustrated in Fig. 14. The width of the pull distribution as a function of the top quark mass is shown in Fig. 15. It is seen that the pull widths are slightly larger than 1 (1.042 ± 0.014). This is because this technique assumes that all events are from $t\bar{t}$ signal. When backgrounds, other decay channels, or extra gluon radiation contaminate the data sample, our assumption is violated and the reported uncertainties will not necessarily be correct. This effect is observed in the pull width. Therefore we correct the final statistical uncertainty in order to have a pull width equal to 1, corresponding to 68% coverage in Gaussian statistics, by scaling the reported uncertainties. The scale factor of 1.04 is extracted by fitting the pull width over the full range of true top quark mass. After applying the mapping function and scaling the statistical uncertainty, we conclude that the top quark mass is reconstructed without bias, over a wide range of input masses.

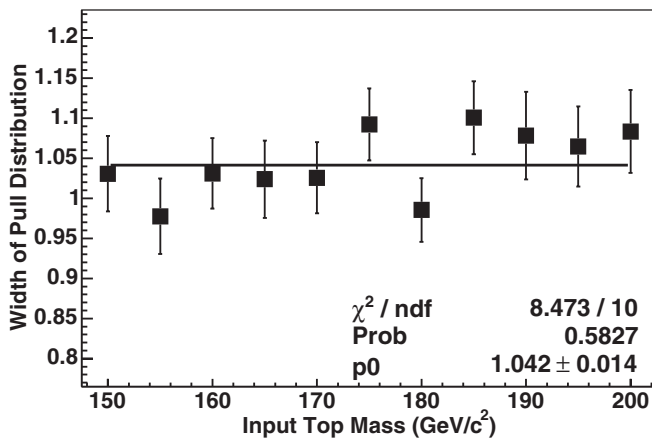


FIG. 15. The width of the pull distribution as a function of the input top quark mass is consistent with a horizontal line fit ($p_0 = 1.042$), as shown in the figure.

X. THE RESULTS FROM THE DATA

We have 63 $t\bar{t}$ candidate events passing the event selection criteria. The joint likelihood of these events is shown in Fig. 16. From the fit, we obtain $M_{\text{top}} = 171.8^{+2.2}_{-2.0} \times$ (stat. only) GeV/c^2 , assuming there is no background. We then apply the mapping function to remove the mass-pulling effect of the background. Figure 17 shows the extracted top mass as a function of the background fraction. The top quark mass changes by $+1.4 \text{ GeV}/c^2$ for a background fraction of 14.5%.

For the final result, we use the estimated 14.5% background fraction, which gives $M_{\text{top}} = 173.2^{+2.6}_{-2.4} \times$ (stat. only) GeV/c^2 . The statistical uncertainty is also scaled by the slope of the mapping function mass shift extracted from Fig. 13 and by 1.04 from the pull width in Fig. 15. Figure 18 shows the likelihood distribution for

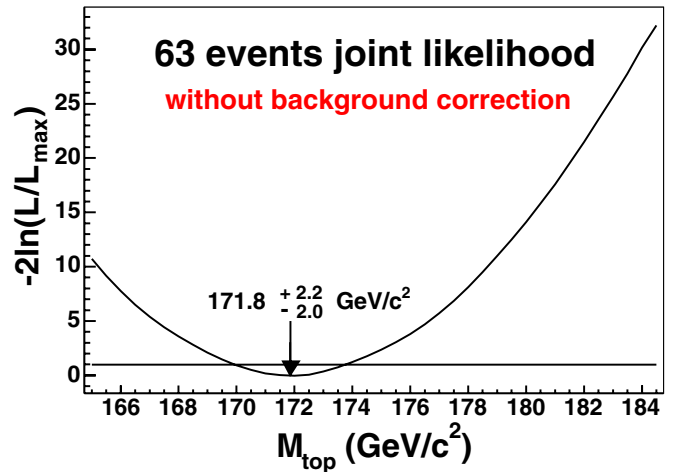


FIG. 16 (color online). The joint negative log likelihood distribution of the 63 events observed in the data. The fit gives $M_{\text{top}} = 171.8^{+2.2}_{-2.0} \text{ GeV}/c^2$, before any corrections.

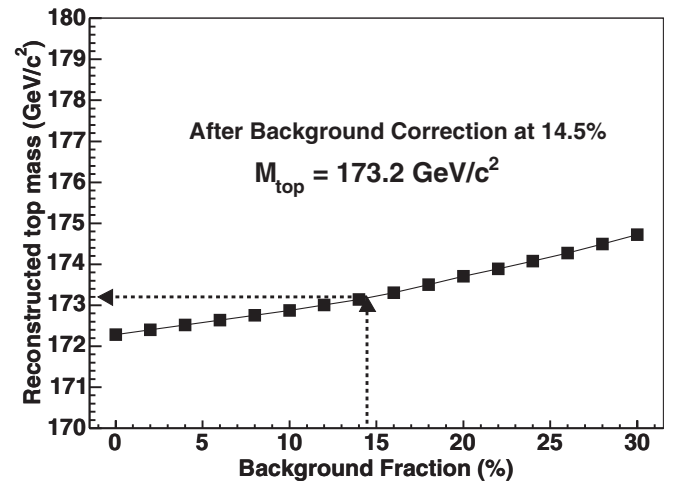


FIG. 17. Extracted top quark mass using the mapping function as a function of the background fraction.

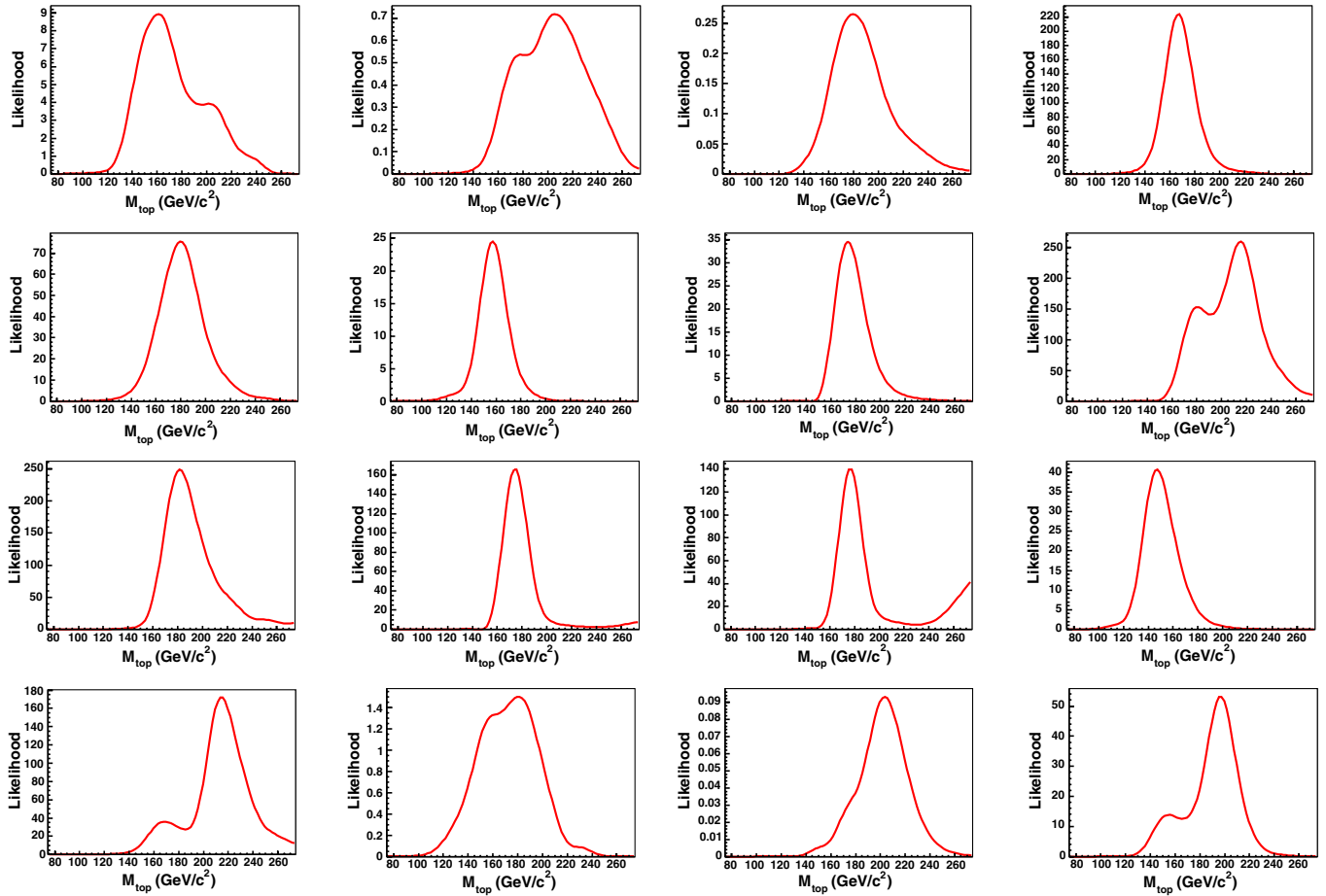


FIG. 18 (color online). Event likelihood distributions as a function of the top quark mass for the 16 double b -tagged events in the data.

each of the 16 data events containing two b -tagged jets. Some of these events have two or three peaks because we sum up all combinations, each of which could produce a different maximum likelihood point. For these 16 events, backgrounds are expected to be small (~ 1.4 events) since two b jets are tagged.

To test how likely the reported statistical uncertainty is, we generated a set of Monte Carlo pseudoexperiments at a top quark mass of $172.5 \text{ GeV}/c^2$ (the closest mass sample to the measured mass), with the number of events in each subsample equal to that observed in the data. Figure 19 shows the expected negative and positive statistical uncertainties. The arrows indicate the statistical uncertainties for the fit to the data. The probability of having a smaller uncertainty than that from data is estimated to be 19%.

As a consistency check, the top quark mass is measured using different subsamples to ensure the robustness of the final result. The analysis procedure applied to these measurements is the same as the one used for the entire data sample. Figure 20 shows the resulting top quark mass for the various categories. Comparisons are made by splitting the events into (1) an electron and a muon channel, (2) lep-

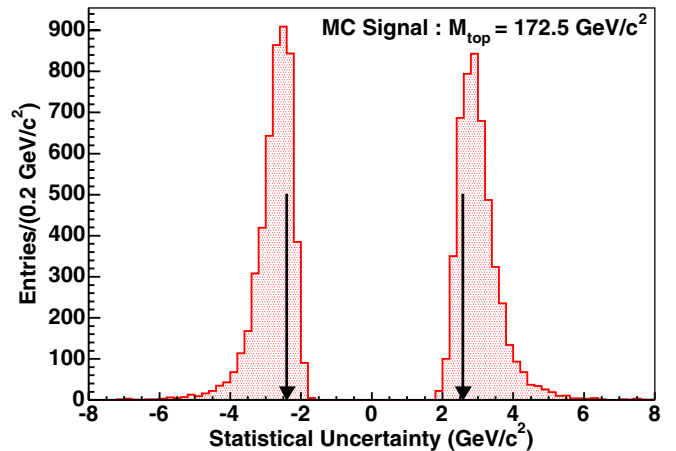


FIG. 19 (color online). The expected positive and negative statistical uncertainties from pseudoexperiments using $172.5 \text{ GeV}/c^2$ $t\bar{t}$ Monte Carlo samples with the same number of events as in the data. The arrows indicate the positive and negative uncertainties for the data. Nineteen percent of the pseudoexperiments have smaller uncertainties than those in the data.

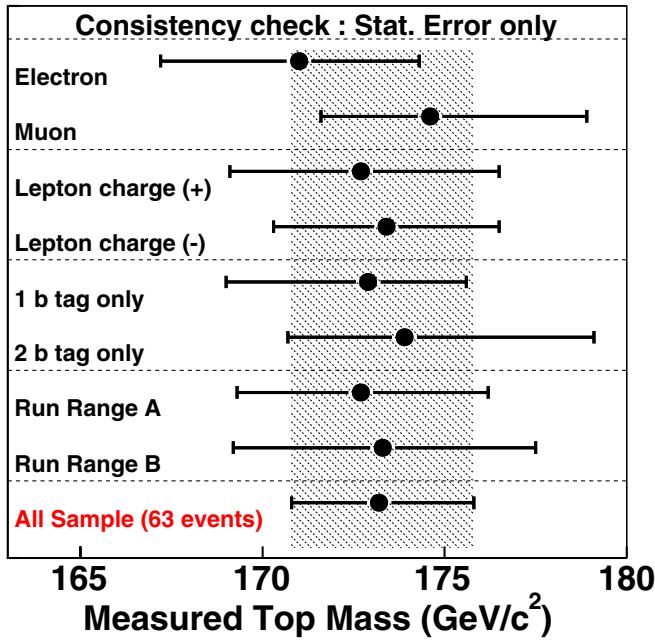


FIG. 20 (color online). Consistency checks: Comparisons between (1) electron and muon channels, (2) lepton charge (\pm), (3) one b -tag and two b -tag events, and (4) run period A which collected data until September 2003 and run period B which is after September 2003. The corresponding integrated luminosities are roughly the same between the two run ranges. Each point includes the statistical uncertainty only.

ton charge (\pm), (3) 1 b -tag and 2 b -tag events, and (4) run period A which collected data until September 2003 and run period B with data accumulated after that date. The corresponding integrated luminosities are roughly the same for the two run ranges. The same mapping function is used to estimate the mass in each category using the expected background fraction of 14.5% except that a background fraction of 9% (1.4/16) is used for 2 b -tag events in category (3). 1.4 and 16 are the expected number of background 2 b -tag events and the number of 2 b -tag events observed in the data, respectively. Although inconsistencies would indicate the presence of new physics in this mode, or perhaps problems with the analysis method, the Monte Carlo modeling, or detector performance, all results are consistent with each other and with the default measurement.

XI. CROSS CHECKS

In order to ensure that the method, calibrated by Monte Carlo samples, describes the data correctly as well as to check how well the Monte Carlo itself models the data, we compare various variables for the data with the Monte Carlo predictions for combined signal and background with regard to (1) the absolute likelihood, (2) the maximum likelihood top quark mass, (3) the maximum likelihood hadronic W mass, and (4) transfer functions.

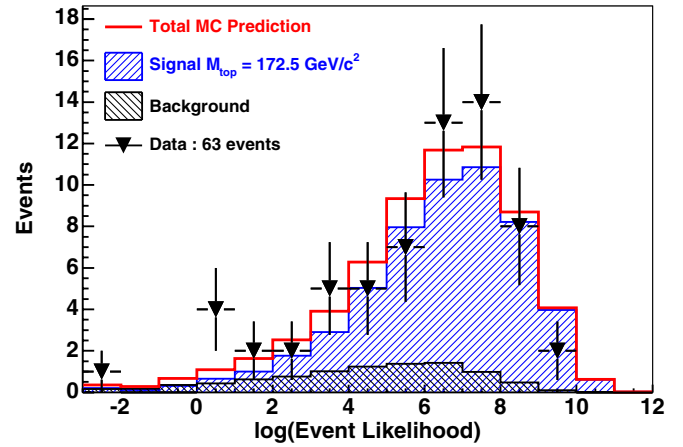


FIG. 21 (color online). Event likelihood distribution. The number of signal and background events is normalized to 63, the number of observed events. The Monte Carlo signal, background, and the combined predictions are shown as histograms. The triangles are the 63 data events.

The normalization of these comparisons is done in the same way, using the expected numbers of events of 9.2 for background and 53.8 for the signal, giving the observed 63 events in total.

A. Absolute likelihood value

Although the absolute value of the likelihood in DLM is arbitrary, we can compare the Monte Carlo with the data. The signal likelihood for the i th event is defined as

$$L_{\text{event}}^i = \int L^i(M) dM, \quad (39)$$

where the integration is over the search region 155–195 GeV/c^2 . Figure 21 shows the comparison of the log of the event likelihoods in the data and the Monte Carlo samples. We find good agreement between the data and Monte Carlo samples.

B. Maximum likelihood top quark mass

A second check uses the event-by-event maximum likelihood mass. We show this quantity for each event in Fig. 22. The signal Monte Carlo sample used for the comparison is generated with $M_{\text{top}} = 172.5 \text{ GeV}/c^2$, close to the central value from the data. The combined background distribution has a peak around 150–160 GeV/c^2 , while the signal events peak at the input value of 172.5 GeV/c^2 . The Monte Carlo prediction agrees well with the data.

C. Hadronic W mass ($W \rightarrow jj$)

We assume that the top quark always decays to a b quark and a real W boson. Therefore, in the top quark mass likelihood, we fix the W mass at 80.4 GeV/c^2 . To check this, we remove the constraint in the likelihood on the mass

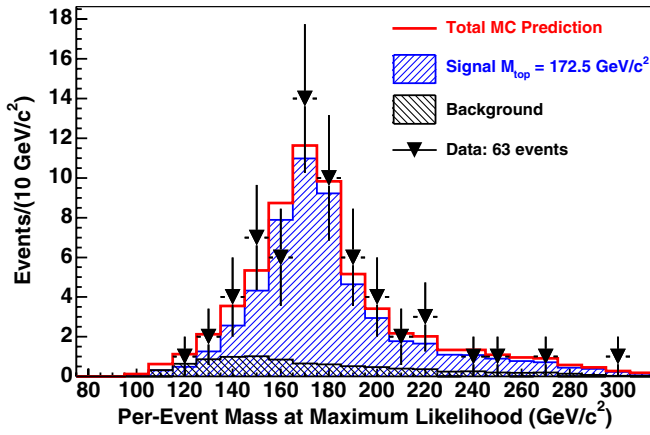


FIG. 22 (color online). The maximum likelihood mass for each event in the data compared to Monte Carlo. The signal Monte Carlo sample is for $M_{\text{top}} = 172.5 \text{ GeV}/c^2$.

of the W that decays into two jets and instead constrain the top quark mass to $172.5 \text{ GeV}/c^2$. Then, in each event, the invariant mass of the two jets assigned to the W at the maximum likelihood point is plotted. Figure 23 shows the comparison between the data and Monte Carlo. We conclude that the dijet mass is consistent with that expected from Monte Carlo $t\bar{t}$ events.

D. Validation of transfer functions

The transfer function is checked by comparing the data and the simulation directly. This is important because we rely on the Monte Carlo simulation for the relation between partons and jets. The energy scale of the jets is understood to $\sim 3\%$, with possible biases taken into account through the systematic uncertainty on the top quark mass. However the resolution and even the scale itself for this specific

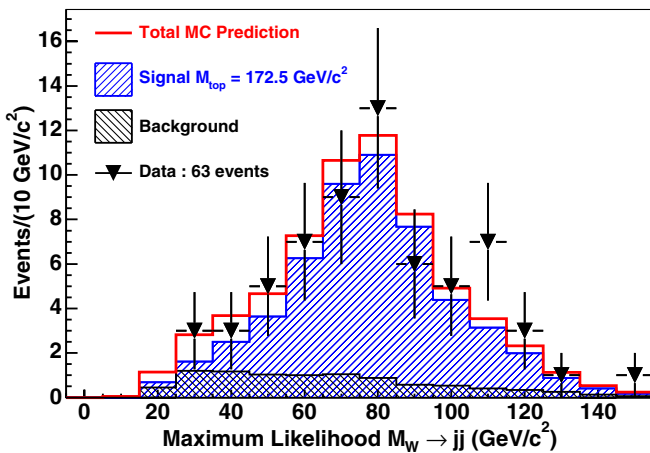


FIG. 23 (color online). Dijet ($W \rightarrow jj$) invariant mass distribution for the maximum likelihood solution for signal ($M_{\text{top}} = 172.5 \text{ GeV}/c^2$) and background, normalized to the expected number of events. The triangles show the 63 data events.

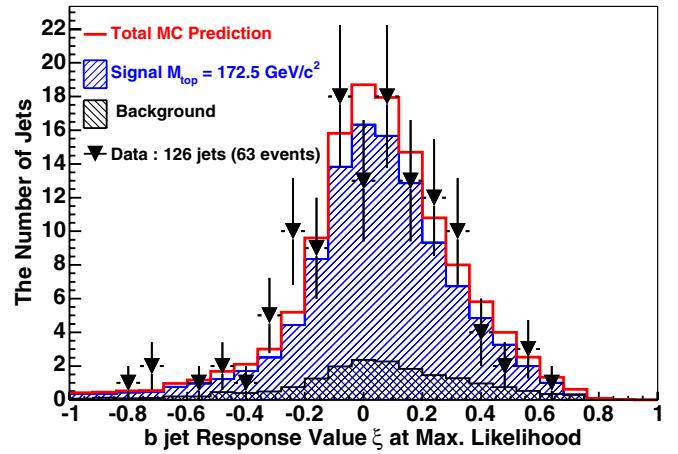


FIG. 24 (color online). Comparison of the b -jet response variable ξ between the data (triangles) and the simulation [histograms show signal, background, and total (= signal + background)]. The means and resolutions are summarized in Table II.

physics process should be checked. To do this, the response variable ξ is selected at the maximum likelihood point for each event. Since each time the likelihood is calculated we assign which jet corresponds to which parton, we can extract the response variables for “jets assigned as b quarks” and “jets assigned as W daughter jets.” These distributions will, of course, include misassignments and gluon contamination, but by comparing the Monte Carlo and the data directly, it is possible to check whether the transfer functions are well modeled. Monte Carlo studies have shown that the mean value of the ξ distribution is slightly different for signal and background, and the resolution of the background is much wider than for the signal

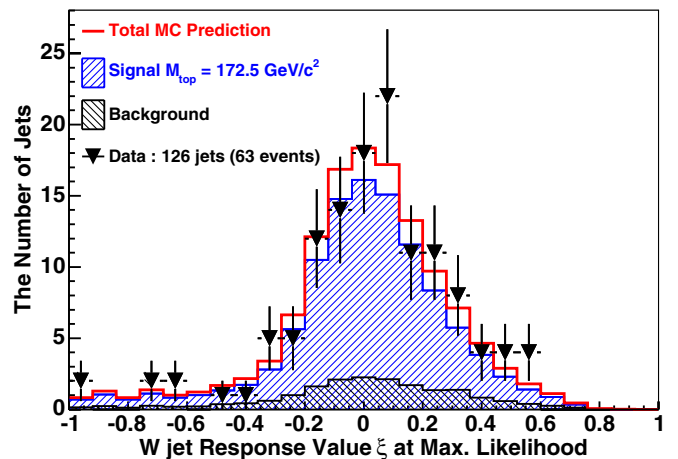


FIG. 25 (color online). Comparison of the W -jet response variable ξ between the data (triangles) and the simulation [histograms show signal, background, and total (= signal + background)]. The means and resolutions are summarized in Table II.

TABLE II. Summary of the mean and RMS of the response variables ξ for the data and the Monte Carlo in Figs. 24 and 25.

	<i>b</i> jet		<i>W</i> jet	
	Mean	RMS	Mean	RMS
MC	0.044 ± 0.002	0.264 ± 0.002	0.012 ± 0.002	0.280 ± 0.002
Data	0.039 ± 0.022	0.263 ± 0.018	0.022 ± 0.026	0.281 ± 0.020

sample. The direct comparisons between data and MC are shown in Figs. 24 and 25 for *b* jets and *W* jets, respectively. Since in each event there are two *b* jets and two *W* jets, the number of data entries in these plots is twice the number of events (63). As a summary, the mean and RMS are listed in Table II. The good agreement indicates that the jet energy scale is well calibrated and no additional systematic uncertainty is needed beyond those from generic jet energy corrections. This test has the potential to further constrain the jet energy scale. In the future, as the integrated luminosity increases, we can use this together with the hadronic $W \rightarrow jj$ mass to reduce the jet energy scale uncertainty. Indeed, CDF has recently used the dijet mass (hadronic *W* mass) to reduce the jet energy scale systematic uncertainty in the template top quark mass analysis [16].

XII. THE SYSTEMATIC UNCERTAINTY

We have performed a number of studies of systematic uncertainties. For each source of uncertainty, we change the input sample and estimate the impact on the reconstructed top quark mass based on a number of pseudoexperiments using Monte Carlo simulations where the input top quark mass is the Run I Tevatron average, $178 \text{ GeV}/c^2$ [53]. The reconstructed mass from each input sample for the various systematic sources is calculated by the same procedure as applied to the data sample; i.e., likelihood computations, followed by the mapping function for a background fraction of 14.5%. These masses are compared to the nominal mass from HERWIG or PYTHIA, depending on the source. The shift in the mean from a Gaussian fit over a large number of pseudoexperiments is taken as the systematic uncertainty.

A. Jet energy scale

With regard to the jet energy corrections, we consider three systematic sources: first the generic corrections calibrated by the QCD dijet process, second the transfer functions for *b* and *W* daughter jets from top decay, and third the *b*-jet energy scale.

First we evaluate the impact on the top quark mass from systematic uncertainties in the generic jet energy corrections. The details of the generic jet energy corrections are described in Sec. IV B. The relative, absolute energy scale (hadron jet modeling), and out-of-cone corrections have uncertainties of roughly 1%, 2%, and 2.5%, respectively. We apply a $\pm 1\sigma$ shift to both signal and background events

and make event selection cuts on the shifted samples. The reconstructed masses are then calculated by the DLM procedure. We take half the difference between the means of the $\pm 1\sigma$ distributions. Table III lists the uncertainties from individual corrections. The total uncertainty is taken to be the quadrature sum of these uncertainties and is found to be $\pm 3.0 \text{ GeV}/c^2$.

Second is the systematic uncertainty from modeling of the transfer functions. In Sec. XI, the TF is checked by comparing the Monte Carlo simulation with the data and found to be consistent. Therefore we only account for the difference of TF's between PYTHIA and HERWIG. We make two sets of TF's, one each from PYTHIA and HERWIG. They are applied to the same Monte Carlo sample, HERWIG with $M_{\text{top}} = 178 \text{ GeV}/c^2$. The difference between the two is found to be $0.2 \text{ GeV}/c^2$.

The last systematic related to the jet energy scale arises from the *b*-jet specific energy scale. The light quark jet scale is set by the generic corrections which are deduced using samples that are mainly light quark and gluon jets. In addition, the sensitivity of the top mass to the light quark jet energy scale is reduced by the *W* mass constraint in the likelihood. On the other hand, the top quark mass is very sensitive to the *b*-jet energy scale, so its additional uncertainty has to be estimated. We consider three possible sources: (1) *b*-quark decay properties, (2) fragmentation properties, and (3) different color flow.

The *B* meson semileptonic branching ratios are varied in the simulation by 3% ($30\% \pm 3\%$), corresponding approximately to the uncertainty in the current world average [53], to estimate its impact on the *b*-jet energy scale. We find that the total uncertainty on *b*-jet response is 0.4%, which translates to a top quark mass difference of $0.4 \text{ GeV}/c^2$. Using the CERN LEP [54,55] and SLC [56] results from large $Z \rightarrow b\bar{b}$ data sets, we constrain the possible fragmentation models in Monte Carlo calculations by changing the Peterson parameter [57] to match the

TABLE III. The systematic uncertainties on the top quark mass for each jet energy systematic source.

Jet energy systematic	$\Delta M_{\text{top}} \text{ GeV}/c^2$
Response relative to central scale	0.6
Modeling of hadron jets (absolute scale)	2.0
Modeling of parton showers (out-of-cone)	2.2
Total systematic due to jet energy scale	3.0

experimental results within their uncertainties. The variations introduce an additional uncertainty of $\pm 0.4 \text{ GeV}/c^2$. For color flow modeling, we vary the parameters of the algorithms used to generate color flow in both PYTHIA and HERWIG. The amount of ambiguous energy, i.e., energy that cannot be assigned to the b jet or the initial-state parton due to the color connection, is estimated to be 3% of the b -jet energy scale. By considering large variations of the parameter related to color flow modeling, the amount of ambiguous energy changes by 0.3% of the total b -jet energy, corresponding to $\pm 0.3 \text{ GeV}/c^2$ in the top quark mass.

These three contributions are added in quadrature, and the resulting $\pm 0.6 \text{ GeV}/c^2$ is assigned as an additional systematic uncertainty due to the modeling of the b -quark energy scale.

B. Initial- and final-state hard radiation

Initial- and final-state gluon radiation (ISR and FSR) affect the top quark mass measurement. ISR produces extra jets that can be misidentified as a $t\bar{t}$ daughter, while FSR can cause a final-state quark jet energy to be measured low. To evaluate the level of ISR, Drell-Yan dilepton events (ee and $\mu\mu$) are used since there is no FSR and they are produced via $q\bar{q}$ annihilation, the dominant production mechanism for $t\bar{t}$ at the Tevatron (85% at next-to-leading order). The average dilepton p_T , $\langle p_T \rangle$, which reflects the size of ISR activity, is shown in Fig. 26 as a function of the dilepton mass squared. A logarithmic dependence is seen between the two. By extrapolating to the energy scale of $t\bar{t}$ production, we find the allowed range for $\langle p_T \rangle$. Two PYTHIA Monte Carlo samples are made with parameters adjusted to cover the range: one with $\Lambda_{\text{QCD}} = 73 \text{ MeV}$,

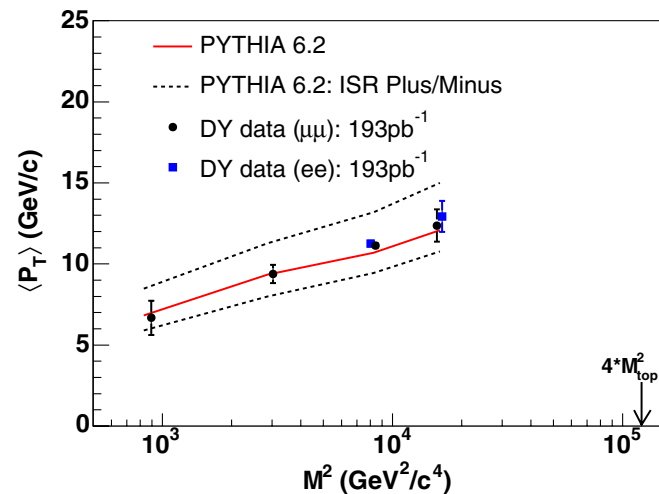


FIG. 26 (color online). The average p_T of dilepton events shows a logarithmic dependence on the dilepton invariant mass squared. The data are compared with PYTHIA samples created with nominal settings as well as those with increased and decreased ISR activity.

$K = 2.0$ and the other with $\Lambda_{\text{QCD}} = 292 \text{ MeV}$, $K = 0.5$ for $-1\sigma_{\text{ISR}}$ and $+1\sigma_{\text{ISR}}$, respectively, where K is a scale factor applied to the transverse momentum scale. Corresponding curves are also shown in Fig. 26. This yields an uncertainty of $\pm 0.4 \text{ GeV}/c^2$. Since both ISR and FSR are controlled by the same DGLAP evolution equation, the same variations of Λ_{QCD} and K are used to generate FSR systematic samples by varying only FSR modeling. This results in a $\pm 0.5 \text{ GeV}/c^2$ variation in the top quark mass.

C. Parton distribution functions

For the parton distribution functions, we add in quadrature uncertainties derived from two sources: differences from 20 pairs of CTEQ6M [58] uncertainty eigenvectors ($\pm 1\sigma$), and MRST [59] with two different Λ_{QCD} values (300 and 228 MeV). The result is an uncertainty of $\pm 0.5 \text{ GeV}/c^2$, of which $0.45 \text{ GeV}/c^2$ comes from the 20 eigenvectors.

Both the PDF and ISR systematics, which impact the p_T of the $t\bar{t}$ system, reflect the sensitivity of the DLM method to the production mechanism. To make an extreme test of this, we created a signal Monte Carlo sample of $t\bar{t}$ resonance production in which $175 \text{ GeV}/c^2$ top quarks are produced from the decay of a $700 \text{ GeV}/c^2$ resonance. In this sample, the top quark decay properties are the same as those in the SM. The shifted mass is found to be $2.0 \text{ GeV}/c^2$, demonstrating that the method is relatively insensitive to major variations in the production mechanism even though we use the SM $t\bar{t}$ production matrix element in the event likelihood. This is because the most sensitive factor in the likelihood is the top quark propagator rather than the production and decay matrix elements.

D. Other systematic uncertainties

Possible bias in the Monte Carlo generator is estimated by comparing PYTHIA and HERWIG. HERWIG deals with spin correlations in the production and decay of $t\bar{t}$, while PYTHIA does not. Another difference between the two is the fragmentation model, where PYTHIA uses the string model while HERWIG adopts the cluster model. We estimate the associated uncertainty to be $\pm 0.3 \text{ GeV}/c^2$ by taking the difference of the reconstructed masses between PYTHIA and HERWIG using the same mapping function extracted from HERWIG. Another systematic uncertainty comes from the mapping function, for which we use a background fraction of 14.5%. The uncertainty on this fraction is $\pm 2.9\%$ from the uncertainty in the mean expected background of ± 1.8 events as shown in Table I. From a series of pseudoexperiments, by changing the background fraction by $\pm 2.9\%$, we estimate this uncertainty to be $\pm 0.2 \text{ GeV}/c^2$. The statistical uncertainty on the expected number of background events (9.2) is already taken into account by the correction obtained from the width of pull distribution discussed in Sec. IX C because the expected

TABLE IV. The summary of systematic uncertainties.

Source	$\Delta M_{\text{top}} \text{ GeV}/c^2$
Jet energy corrections	3.0
Transfer function	0.2
ISR	0.4
FSR	0.5
PDFs	0.5
Generator	0.3
Background fraction	0.2
Background modeling	0.4
b -jet energy modeling	0.6
b -tagging	0.2
Total	3.2

number of background events has been Poisson fluctuated in the pseudoexperiments.

The uncertainty due to background modeling, $\pm 0.4 \text{ GeV}/c^2$, comes from two sources: We evaluate the difference between the reconstructed masses obtained by using only one of the individual background process, rather than using combined background. Then the maximum difference among the major background sources (W + heavy flavor quarks, W + mistagged jets, non- W background) is used. The other source is the variation with different choices of the Q^2 scale ($4M_W^2$, M_W^2 , $M_W^2/4$, and $M_W^2 + P_{TW}^2$) which is the characteristic energy scale of the hard scattering process using the ALPGEN Monte Carlo program. This takes into account possible variations in the background composition. Finally, as described in Sec. IV, the b -tagging efficiency is different in data and Monte Carlo. Only the jet E_T dependence of the tagging efficiency is important in the mass analysis. By varying the slope of the efficiency as a function of E_T by $\pm 1\sigma$, we find the top quark mass shifts by $\pm 0.2 \text{ GeV}/c^2$. The uncertainty due to the finite statistics of the non- W data sample and the Monte Carlo samples used to make the mapping functions is negligible.

E. Summary of systematic uncertainties

The systematic uncertainties are summarized in Table IV. The largest one comes from the uncertainty in the jet energy measurement. The sum in quadrature of all the systematic uncertainties is $3.2 \text{ GeV}/c^2$.

XIII. CONCLUSION

Using the dynamical likelihood method, we measure the top quark mass to be

$$M_{\text{top}} = 173.2_{-2.4}^{+2.6} \text{ (stat.)} \pm 3.2 \text{ (syst.) GeV}/c^2$$

$$= 173.2_{-4.0}^{+4.1} \text{ GeV}/c^2$$

from 63 events, corresponding to an integrated luminosity of 318 pb^{-1} accumulated in the CDF Run II experiment. By using the maximal information from the $t\bar{t}$ production mechanism and assuming the validity of the SM, a reduction of the statistical uncertainty is obtained. The precision of this single measurement, in fact, is slightly better than the Run I world average, and the result is consistent with other recent measurement by CDF [16], which provided the best single measurement ($173.5_{-3.8}^{+3.9} \text{ GeV}/c^2$) using the template technique with a dijet W mass constraint to reduce the jet energy scale uncertainty. The current DLM analysis technique uses the jet energy scale determined with generic jet samples. However, as the luminosity increases, a reduction of the dominant systematic uncertainty, due to the jet energy scale, is crucial. DLM will be able to further constrain the jet energy scale using the hadronic $W \rightarrow jj$ mass in $t\bar{t}$ events as done in [16]. We expect that other systematics also can be improved as the size of control samples increases. A reduced top quark mass uncertainty with an increased data sample size will contribute to the detailed understanding of the electroweak interaction as well as to the search for physics beyond the standard model.

ACKNOWLEDGMENTS

We thank the Fermilab staff and the technical staffs of the participating institutions for their vital contributions. This work was supported by the U.S. Department of Energy and National Science Foundation; the Italian Istituto Nazionale di Fisica Nucleare; the Ministry of Education, Culture, Sports, Science and Technology of Japan; the Natural Sciences and Engineering Research Council of Canada; the National Science Council of the Republic of China; the Swiss National Science Foundation; the A.P. Sloan Foundation; the Bundesministerium für Bildung und Forschung, Germany; the Korean Science and Engineering Foundation and the Korean Research Foundation; the Particle Physics and Astronomy Research Council and the Royal Society, UK; the Russian Foundation for Basic Research; the Comisión Interministerial de Ciencia y Tecnología, Spain; in part by the European Community's Human Potential Programme under Contract No. HPRN-CT-2002-00292; and the Academy of Finland.

- [1] F. Abe *et al.* (CDF Collaboration), Phys. Rev. Lett. **82**, 2808 (1999).
- [2] B. Abbott *et al.* (D0 Collaboration), Phys. Rev. D **60**, 052001 (1999).
- [3] T. Affolder *et al.* (CDF Collaboration), Phys. Rev. D **63**, 032003 (2001).
- [4] B. Abbott *et al.* (D0 Collaboration), Phys. Rev. D **58**, 052001 (1998).
- [5] F. Abe *et al.* (CDF Collaboration), Phys. Rev. Lett. **79**, 1992 (1997).
- [6] V. M. Abazov *et al.* (D0 Collaboration), Phys. Lett. B **606**, 25 (2005).
- [7] V. M. Abazov *et al.* (D0 Collaboration), Nature (London) **429**, 638 (2004).
- [8] P. Azzi *et al.*, hep-ex/0404010, <http://tevewwg.fnal.gov>.
- [9] LEP ElectroWeak Working Group, hep-ex/0509008.
- [10] K. Kondo, J. Phys. Soc. Jpn. **57**, 4126 (1988).
- [11] K. Kondo, J. Phys. Soc. Jpn. **60**, 836 (1991).
- [12] K. Kondo, T. Chikamatsu, and S. H. Kim, J. Phys. Soc. Jpn. **62**, 1177 (1993).
- [13] K. Kondo, Waseda University, RISE Technical Report No. 05-01, 2005 (hep-ex/0508035).
- [14] V. M. Abazov *et al.* (D0 Collaboration), Phys. Lett. B **617**, 1 (2005).
- [15] R. H. Dalitz and G. R. Goldstein, Phys. Rev. D **45**, 1531 (1992).
- [16] A. Abulencia *et al.* (CDF Collaboration), Phys. Rev. D **73**, 032003 (2006).
- [17] A. Abulencia *et al.* (CDF Collaboration), Phys. Rev. Lett. **96**, 022004 (2006).
- [18] F. Abe *et al.* (CDF Collaboration), Phys. Rev. Lett. **74**, 2626 (1995); S. Abachi *et al.* (D0 Collaboration), Phys. Rev. Lett. **74**, 2632 (1995).
- [19] D. Acosta *et al.* (CDF Collaboration), Phys. Rev. D **72**, 052003 (2005); V. Abazov *et al.* (D0 Collaboration), Phys. Lett. B **626**, 35 (2005).
- [20] A. Abulencia *et al.* (CDF Collaboration), hep-ex/0511023; V. Abazov *et al.* (D0 Collaboration), Phys. Rev. D **72**, 011104 (2005).
- [21] D. Acosta *et al.* (CDF Collaboration), Phys. Rev. Lett. **95**, 102002 (2005).
- [22] D. Acosta *et al.* (CDF Collaboration), Phys. Rev. D **71**, 032001 (2005); R. Blair *et al.* (CDF Collaboration), Fermilab Report No. FERMILAB-PUB-96/390-E, 1996.
- [23] T. Affolder *et al.*, Nucl. Instrum. Methods Phys. Res., Sect. A **526**, 249 (2004).
- [24] C. S. Hill *et al.*, Nucl. Instrum. Methods Phys. Res., Sect. A **530**, 1 (2004).
- [25] A. Sill *et al.*, Nucl. Instrum. Methods Phys. Res., Sect. A **447**, 1 (2000).
- [26] T. Affolder *et al.*, Nucl. Instrum. Methods Phys. Res., Sect. A **453**, 84 (2000).
- [27] L. Balka *et al.*, Nucl. Instrum. Methods Phys. Res., Sect. A **267**, 272 (1988).
- [28] S. Bertolucci *et al.*, Nucl. Instrum. Methods Phys. Res., Sect. A **267**, 301 (1988).
- [29] M. G. Albrow *et al.*, Nucl. Instrum. Methods Phys. Res., Sect. A **480**, 524 (2002).
- [30] G. Ascoli *et al.*, Nucl. Instrum. Methods Phys. Res., Sect. A **268**, 33 (1988).
- [31] T. Dorigo *et al.*, Nucl. Instrum. Methods Phys. Res., Sect. A **461**, 560 (2001).
- [32] G. Marchesini *et al.*, Comput. Phys. Commun. **67**, 465 (1992); G. Corcella *et al.*, J. High Energy Phys. 01 (2001) 010.
- [33] T. Sjostrand *et al.*, Comput. Phys. Commun. **135**, 238 (2001).
- [34] J. Pumplin *et al.*, J. High Energy Phys. 07 (2002) 012.
- [35] P. Avery, K. Read, and G. Trahern, Cornell Internal Report No. CSN-212, 1985 (unpublished).
- [36] M. L. Mangano *et al.*, J. High Energy Phys. 07 (2003) 001.
- [37] E. Gerchtein and M. Paulini, econf C0303241, TUMT005, 2003 (physics/0306031).
- [38] R. Brun and F. Carminati, CERN Programming Library Long Writeup, Report No. W5013, 1993 (unpublished).
- [39] G. Grindhammer, M. Rudowicz, and S. Peters, Nucl. Instrum. Methods Phys. Res., Sect. A **290**, 469 (1990).
- [40] A. Abulencia *et al.* (CDF Collaboration), hep-ex/0508029.
- [41] F. Abe *et al.* (CDF Collaboration), Phys. Rev. D **45**, 1448 (1992).
- [42] F. Abe *et al.* (CDF Collaboration), Phys. Rev. Lett. **68**, 1104 (1992).
- [43] A. Bhatti *et al.*, hep-ex/0510047.
- [44] T. Affolder *et al.* (CDF Collaboration), Phys. Rev. D **64**, 032002 (2001).
- [45] D. Acosta *et al.* (CDF Collaboration), Phys. Rev. D **71**, 052003 (2005).
- [46] J. M. Campbell and R. K. Ellis, Phys. Rev. D **60**, 113006 (1999).
- [47] B. W. Harris, E. Laenen, L. Phaf, Z. Sullivan, and S. Weinzierl, Phys. Rev. D **66**, 054024 (2002).
- [48] M. Cacciari *et al.*, J. High Energy Phys. 04 (2004) 68.
- [49] K. Hagiwara *et al.*, Phys. Rev. D **66**, 010001 (2002).
- [50] R. K. Ellis, W. J. Stirling, and B. R. Webber, *QCD and Collider Physics*, Cambridge Monographs on Particle Physics, Nuclear Physics and Cosmology (Cambridge University Press, Cambridge, England, 1996), p. 348; R. K. Ellis, in *Strong Interactions and Gauge Theories*, edited by J. Tran Thanh Van (Frontières, Gif-sur-Yvette, 1986), p. 339.
- [51] M. Gluck, J. F. Owens, and E. Reya, Phys. Rev. D **17**, 2324 (1978); B. Combridge, Nucl. Phys. **151**, 429 (1979).
- [52] G. Mahlon and S. Parke, Phys. Rev. D **53**, 4886 (1996); Phys. Lett. B **411**, 173 (1997).
- [53] S. Eidelman *et al.*, Phys. Lett. B **592**, 1 (2004).
- [54] A. Heister *et al.* (ALEPH Collaboration), Phys. Lett. B **512**, 30 (2001).
- [55] G. Abbiendi *et al.* (OPAL Collaboration), Eur. Phys. J. C **29**, 463 (2003).
- [56] K. Abe *et al.* (SLD Collaboration), Phys. Rev. D **65**, 092006 (2002).
- [57] C. Peterson, D. Schlatter, I. Schmitt, and P. M. Zerwas, Phys. Rev. D **27**, 105 (1983).
- [58] D. Stump *et al.*, J. High Energy Phys. 10 (2003) 046.
- [59] A. D. Martin *et al.*, Eur. Phys. J. C **14**, 133 (2000).